Chemical abundances of globular clusters in NGC 5128 (Centaurus A)

Hernandez, Svea; Larsen, Søren; Trager, Scott; Kaper, Lex; Groot, Paul

Published in:
Monthly Notices of the Royal Astronomical Society

DOI:
10.1093/mnras/sty519

Publication date:
2018

Monthly Notices
of the
ROYAL ASTRONOMICAL SOCIETY

MNRAS **476,** 5189–5215 (2018) doi:10.1093/mnras/sty519
Advance Access publication 2018 February 27

Chemical abundances of globular clusters in NGC 5128 (Centaurus A)

Svea Hernandez,[1]★ Søren Larsen,[1] Scott Trager,[2] Lex Kaper[3] and Paul Groot[1]

[1]*Department of Astrophysics/IMAPP, Radboud University, PO Box 9010, NL-6500 GL Nijmegen, the Netherlands*
[2]*Kapteyn Astronomical Institute, University of Groningen, Postbus 800, NL-9700 AV Groningen, the Netherlands*
[3]*Astronomical Institute Anton Pannekoek, Universiteit van Amsterdam, Postbus 94249, NL-1090 GE Amsterdam, the Netherlands*

Accepted 2018 February 23. Received 2018 February 23; in original form 2018 January 22

ABSTRACT

We perform a detailed abundance analysis on integrated-light spectra of 20 globular clusters (GCs) in the early-type galaxy NGC 5128 (Centaurus A). The GCs were observed with X-Shooter on the Very Large Telescope (VLT). The cluster sample spans a metallicity range of $-1.92 < [Fe/H] < -0.13$ dex. Using theoretical isochrones, we compute synthetic integrated-light spectra and iterate the individual abundances until the best fit to the observations is obtained. We measured abundances of Mg, Ca, and Ti, and find a slightly higher enhancement in NGC 5128 GCs with metallicities $[Fe/H] < -0.75$ dex, of the order of $\sim$0.1 dex, than in the average values observed in the Milky Way (MW) for GCs of the same metallicity. If this α-enhancement in the metal-poor GCs in NGC 5128 is genuine, it could hint at a chemical enrichment history different than that experienced by the MW. We also measure Na abundances in 9 out of 20 GCs. We find evidence for intracluster abundance variations in six of these clusters where we see enhanced $[Na/Fe] > +0.25$ dex. We obtain the first abundance measurements of Cr, Mn, and Ni for a sample of the GC population in NGC 5128 and find consistency with the overall trends observed in the MW, with a slight enhancement (<0.1 dex) in the Fe-peak abundances measured in the NGC 5128.

Key words: galaxies: abundances – galaxies: star clusters: general.

1 INTRODUCTION

There is a bewildering variety of properties in the galaxies we currently observe in the universe. The differences between these objects range from morphology, luminosity, and colour to star formation histories, chemical composition, and kinematics. In order to fully understand how galaxies in our universe evolve, we need to study in detail galaxies of different Hubble types, not just our own.

A very powerful tool to understand the evolution of galaxies is the study of their chemical abundances as a function of time. More specifically, one can obtain a detailed picture of the evolution of galaxies by looking closely at the abundance patterns of different elements observed in various stellar populations. Considering that the chemical composition of the gas reservoirs that form stars is preserved in their atmospheres, one can extract an immense amount of information through the analysis of stars of different ages. Past studies have shown that the stellar abundance ratios can constrain initial mass functions (IMFs) and star formation rates (SFRs, McWilliam 1997; Matteucci 2003).

It is believed that type Ia supernovae (SNe Ia) are the primary sources of Fe and Fe-peak elements in the Galaxy (Nomoto, Iwamoto & Kishimoto 1997). Additionally, it has been established that type II supernovae (SNe II) are instead responsible for the creation of most of the α-elements (O, Mg, Si, S, Ca, and Ti; Woosley & Weaver 1995).

One of the most widely used diagnostics of IMF and SFR is the abundance ratio of α-elements to Fe, [α/Fe]. A top-heavy IMF could lead to enhanced [α/Fe] ratios along with high average metallicities (Matteucci & Brocato 1990). However, similar enhancements in the [α/Fe] ratios can also be the result of a rapid burst of star formation enriching the gas to high metallicities. In the case of our own Milky Way (MW), the enhancement of α-elements in old stellar populations points at a starburst system (Worthey 1998; Matteucci 2003).

Given our proximity to stars in the MW, high-resolution spectroscopy has allowed for abundance studies that provide an incredibly detailed picture of the nucleosynthetic history of our Galaxy. Individual stellar abundances within the MW have assisted in identifying the location and substructures of different populations (e.g. Venn et al. 2004; Pritzl, Venn & Irwin 2005; Reddy, Lambert & Allende Prieto 2006). Even though a limited number of extragalactic abundances of stars in nearby systems, such as the Magellanic Clouds and dwarf galaxies, are also available (e.g. Wolf 1973; Venn 1999; Shetrone, Bolte & Stetson 1999; Tolstoy et al. 2003), to better understand the episodes of star formation in different galaxy types and masses, detailed abundances far beyond the MW and its neighbours in the Local Group are needed.

★ E-mail: s.hernandez@astro.ru.nl

Most of the abundance work beyond the Local Group has been limited by the difficulty in measuring reliable abundances. The majority of the extragalactic (outside of the Local Group) metallicity and abundance measurements come from studies of H II regions in star-forming galaxies (Searle 1971; Lee, Salzer & Melbourne 2004; Stasińska 2005). A known issue with such methods is apparent once we compare the metallicities inferred from different diagnostics. Studies have noticed differences in the inferred metallicities as high as ∼0.7 dex (Kennicutt et al. 2003; Bresolin 2008; Kewley & Ellison 2008; López-Sánchez et al. 2012). Additionally, H II region abundances mainly probe the present-day gas composition, and one cannot access any information on the past evolution of the host galaxy.

For galaxies other than star-forming, different methods are used to study their composition, and star formation histories. For early-type galaxies, several extensive studies have been conducted using absorption line indices as their main resource. Thomas et al. (2005) studied the stellar properties of 124 early-type galaxies deriving metallicities, [α/Fe] ratios, and ages using absorption line indices as well as stellar population models. They find that all three, age, metallicity, and [α/Fe] abundance ratio, correlate with the mass of the galaxy. These results, especially those of the [α/Fe]–mass relation had been anticipated before the work of Thomas et al. (2005) by Worthey, Faber & González (1992), Fisher, Franx & Illingworth (1995), and Kuntschner (2000), amongst others, and verified by Trager et al. (2000), Proctor & Sansom (2002), and Thomas, Maraston & Bender (2002) through stellar population models. Overall, this relation between [α/Fe] and mass observed in earlier studies is consistent with a scenario where higher effective yields from SNe II are expected and observed in more massive galaxies ($>10^{11}$ $M_{\odot}$).

One of the main challenges in obtaining detailed abundances of individual stars in galaxies outside of the Local Group is the fact that at larger distances stars become too faint for this type of analysis. In order to overcome this obstacle, studies are now focusing on star clusters, where one of the assumptions is that the individual populations of stars consist of objects of the same age, and are chemically homogenous. The study of integrated-light observations has allowed for a significant advancement in the field of chemical evolution of distant galaxies. Given that the integrated-light spectra of most star clusters are broadened by several km s^{-1}, one can observe star clusters at much higher resolution (R =20 000–30 000) than galaxies, allowing for the detection of weak lines (15 mÅ). Studies of star clusters, mainly globular clusters (GCs), have shown that these objects trace the properties of the different field star populations in their host galaxies (Colucci et al. 2013; Sakari et al. 2015). More specifically, detailed properties such as metallicity, age, and abundances are powerful tools for constraining theories of GC and galaxy formation (Brodie & Strader 2006).

One of the major highlights in the studies of extragalactic GCs is the presence of subpopulations with two main components, metal poor and metal rich. Until the early 2000s, most of the spectroscopic analysis exploring extragalactic GCs utilized Lick/image dissector scanner indices (Burstein et al. 1984; Worthey et al. 1994; Trager et al. 1998). This technique was originally developed to study the absorption features in low-resolution observations at wavelengths of ∼4000–6400 Å of early-type galaxies to measure the properties of their stellar populations. More optimal methods based on the index system were later developed to be more applicable to GC studies. The bulk of extragalactic spectroscopic measurements of metallicities, ages, and [α/Fe] ratios have been inferred mainly by measuring Lick indices. One of the most extensive and systematic studies of extragalactic GC systems was published by Strader et al. (2005) and spanned a broad range of galaxies from dwarfs to ellipticals. This work showed that both GC subpopulations, metal poor and metal rich, have mean ages similar to those seen in the MW GC system with the implication that the bulk of star formation in spheroids occurred at early ages ($z > 2$).

The general expectation regarding the metal-poor and metal-rich populations of GCs in external galaxies is that the former would show supersolar [α/Fe] ratios given that their formation took place in the early universe when a substantial metal enrichment was yet to happen. Several studies of extragalactic metal-poor GCs appear to have [α/Fe] $\lesssim 0$ (Olsen et al. 2004; Pierce et al. 2005), while others show enhanced [α/Fe]. On the other hand, a study of GCs in early-type galaxies by Puzia et al. (2005), using Lick indices to measure ages, metallicities, and [α/Fe] abundances leads them to conclude that [α/Fe] ratios are on average supersolar with a mean value of $+0.47 \pm 0.06$ dex which points at short star formation time-scales (∼1 Gyr). They also conclude that the progenitor cloud forming these GCs in early-type galaxies would need to have been predominantly enriched by yields from SNe II. The discrepancy between results obtained from different studies of early-type galaxies could be caused by the uncertainties in the simple stellar population (SSP) models used in combination with the wide Lick index bandpasses, making the abundance ratio measurements highly uncertain (Brodie & Strader 2006).

McWilliam & Bernstein (2008) developed a technique to study individual abundances of GCs through the analysis of their integrated light. Their method requires high-resolution observations (R=30 000) and combines information of the Hertzsprung–Russell diagrams of the GC in question, stellar atmospheric models, and synthetic spectra. This technique has been tested and applied to GCs in the MW and the Large Magellanic Cloud (LMC, McWilliam & Bernstein 2008; Cameron 2009; Colucci et al. 2011), and at relatively larger distances (M31 at ∼ 780 kpc, Colucci et al. 2009; Colucci, Bernstein & Cohen 2014; Colucci, Bernstein & McWilliam 2016).

Similar to the concept of McWilliam & Bernstein (2008), Larsen et al. (2012, hereafter L12) created a high-resolution integrated-light technique to measure abundances of star clusters. In contrast to the technique of McWilliam & Bernstein (2008), the method of L12 mainly relies on spectral synthesis and full spectral fitting. Abundance measurements are obtained by fitting relatively broad wavelength ranges containing multiple lines of the element in question. The method of L12 has been used to measure chemical abundances of old stellar populations in the MW, and several dwarf spheroidal (dSph) galaxies (Larsen et al. 2012, 2014; Larsen, Brodie & Strader 2017).

Although the L12 technique was developed using high-dispersion spectroscopic observations, we extended the L12 method to intermediate-resolution spectra (R < 10 000) in Hernandez et al. (2017, 2018). In these studies, we measured detailed abundances of two young massive clusters (YMCs) and overall metallicities of eight YMCs in galaxies ∼5 Mpc away. With techniques like L12 where one is able to study stellar populations in a broad range of ages, from old GCs to young populations (YMCs), and with a slightly less limited spectral resolution range, we can now investigate the chemical evolution of galaxies through a much larger window in space and time than in past studies.

Being the nearest giant early-type galaxy to the MW, NGC 5128 (Centaurus A) is an ideal target to measure detailed abundances from integrated-light spectra of its GCs. In spite of being the nearest giant early-type galaxy, NGC 5128 is still located at a distance of 3.8 Mpc from our Galaxy (Harris, Rejkuba & Harris 2010). Colucci

et al. (2013) initiated a study of the chemical composition of the GC system of NGC 5128 measuring Fe and Ca abundances of 10 different clusters. In their work, Colucci et al. (2013) measured Fe abundances with ranges of $-1.6 < [Fe/H] < -0.2$ dex. A noticeable result from this work was the enhanced [Ca/Fe] ratio for metallicities of $[Fe/H] < -0.4$ dex, which appeared higher than the average values for the GCs in the MW and M31 of the same metallicities. These results implied a different star formation history for NGC 5128 compared to those from the MW and M31.

We perform a detailed abundance analysis on a sample of 20 star clusters distributed throughout NGC 5128. Using the L12 method, along with intermediate-resolution observations, we measure abundances of light (Na) and α elements (Mg, Ca, and Ti), as well as Fe-peak (Cr, Mn, and Ni). This paper is structured as follows. In Section 2, we describe the science observations and data reduction. In Sections 3 and 4, we present the analysis method and results, respectively. Section 5 is used to discuss our findings, and we list our conclusions in Section 6.

2 OBSERVATIONS AND DATA REDUCTION

In this work, we exploit the data taken as part of the Very Large Telescope (VLT) programme 085.B-0107(A) observing 25 bright star clusters in NGC 5128. The exposures are taken with the X-Shooter single target spectrograph (Vernet et al. 2011). The instrument has a broad wavelength coverage, providing data between 3000 and 24 800 Å. X-Shooter's extensive wavelength coverage is possible through its three spectroscopic arms. Each of these arms, ultraviolet-blue (UVB), visible (VIS), and near-IR (NIR), has a full set of optimized optics and detectors. The resolution of the instrument is mainly controlled by the slit width, with resolutions ranging from $R = 3000$ to 17 000. Programme 085.B-0107(A) was executed in 2010 April using slit widths 0.8 arcsec ($R \sim 6200$), 0.7 arcsec ($R \sim 11\,000$), and 0.6 arcsec ($R \sim 6200$) for UVB, VIS, and NIR arm, respectively. The data were taken using the standard nodding mode following an ABBA pattern.

Targets with magnitudes brighter than $V \sim 19$ were selected from the spectroscopically confirmed GC sample by Beasley et al. (2008). This means that our cluster sample mainly covers the brightest component of the GC system in NGC 5128. In Fig. 1, we show in blue circles the full GC sample of Beasley et al. (2008), plotting the V magnitudes as a function of metallicity. We indicate with red stars the cluster sample analysed in this work. In Table 1, we list the target names, coordinates, exposure times, and signal-to-noise (S/N) ratios for the different arms. The S/N values are calculated using wavelength windows of 4550–4750 Å for the UVB, 7350–7500 Å for the VIS data, and 10 400–10 600 Å for the NIR data. We point out that given the low S/N in the NIR data, the work done in this paper focuses on the X-Shooter observations taken with the UVB and VIS arm only. In Fig. 2, we mark the star clusters analysed in this paper.

Using the public release of the X-Shooter pipeline (v2.5.2) along with the European Southern Observatory (ESO) Recipe Execution Tool (ESOREX) v3.11.1, we perform the basic data reduction steps, including bias and dark corrections, flat-fielding, sky subtraction, and wavelength calibration. We take the 2D calibrated exposures and extract the science spectrum using IDL routines by Chen et al. (2014). The code was developed based on optimal extraction principles described in Horne (1986). Once the 1D spectrum is extracted, the code combines the individual orders using the variance-weighted average for overlapping spectral regions. The 1D spectra are flux calibrated using the spectrophotometric standard Feige 110 observed

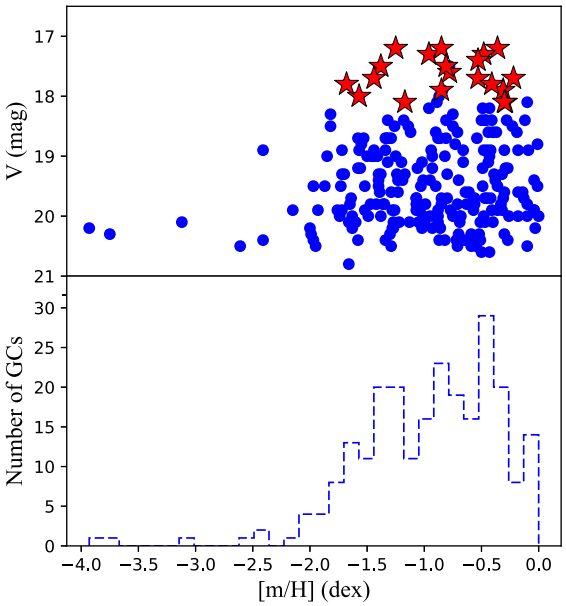

Figure 1. Top panel: V magnitudes as a function of spectroscopic metallicities as measured by Beasley et al. (2008). Blue circles and red stars show the full GC study by Beasley et al. (2008) and the sample studied in this work, respectively. Bottom panel: metallicity distribution (bin widths of ~ 0.13 dex) for the GC system in NGC 5128.

close in time to the science frames. We use the pipeline routine xsh_respon_slit_offset to create response curves for the individual exposures. The response curves use the same bias and master flat frames as those applied to the corresponding science observations, and are corrected for exposure time and atmospheric extinction. It is important to apply the same flat-field frames for both the science and the response curves in order to remove any contemporaneous flat-field features. After the flux calibration, we visually inspect the 1D spectra and find good flux agreement between the UVB and VIS arm. We note that in most of the targets observed in this program, we see strong dichroic features at wavelengths <5700 Å (in the VIS arm). These dichroic features tend to appear in the extracted 1D spectra of the X-Shooter VIS data, with their exact wavelength position varying from exposure to exposure making it rather difficult to remove entirely (Chen et al. 2014). Although our abundance analysis does not require accurate flux calibration, these dichroic features can artificially modify not only the continuum, but also the depth of the intrinsic spectral lines. Given the nature of the dichroic features, we exclude most of the VIS wavelengths <5700 Å in our analysis.

Telluric absorption bands strongly affect our VIS exposures. Observations with wavelengths between 5800–6100 Å, 6800–7400 Å, 7550–7750 Å, 7800–8500 Å, and 8850–10 000 Å, are mainly contaminated by these absorption bands. We correct for this contamination from the Earth's atmosphere using the routines and telluric library developed by the X-Shooter Spectral Library team. Chen et al. (2014) created a correction method based on principal component analysis which depends on their carefully designed telluric library. We apply this correction which reconstructs and removes the strongest telluric absorption as needed. Although we correct our observations for telluric contamination, in our analysis we aim to avoid these regions. We mainly focus our abundance analysis in the UVB wavelengths 4400–5200 Å, and VIS wavelength windows 5670–5700 Å, 6100–6800 Å, 7400–7550 Å, and 8500–8850 Å.

Table 1. X-Shooter observations.

Cluster	RA (J2000)	Dec. (J2000)	t_{exp} (s) UVB	VIS	NIR	S/N (pixel^{-1}) UVB	VIS	NIR
AAT117062	201.378408	−42.83718	1800.0	1780.0	1800.0	29.1	34.0	13.5
HGHH-04	201.256648	−43.15735	1800.0	1780.0	1800.0	12.3	18.1	7.2
HGHH-06	201.342347	−43.04529	1800.0	1780.0	1800.0	14.6	19.2	8.6
HGHH-07	201.521448	−42.94223	1800.0	1780.0	1800.0	25.9	29.4	12.0
HGHH-11	201.228781	−43.0223	1800.0	1780.0	1800.0	16.9	22.4	10.7
HGHH-17	201.416499	−42.93268	1800.0	1780.0	1800.0	24.3	28.1	11.5
HGHH-21	201.470672	−43.09595	1800.0	1780.0	1800.0	18.5	22.7	9.0
HGHH-23	201.476303	−42.99024	1800.0	1780.0	1800.0	28.6	39.6	24.0
HGHH-29	201.167061	−43.30198	1800.0	1780.0	1800.0	12.1	20.0	10.6
HGHH-34	201.41993	−43.3532	1800.0	1780.0	1800.0	13.2	16.7	7.9
HGHH-40	200.927402	−43.16027	1800.0	1780.0	1800.0	8.8	11.1	3.4
HH-080	200.909807	−42.77231	1800.0	1780.0	1800.0	14.9	17.1	5.6
HH-096	201.088942	−43.04287	1800.0	1780.0	1800.0	18.5	21.5	8.2
HHH86-30	201.225916	−42.88951	1800.0	1780.0	1800.0	31.2	37.9	19.8
HHH86-39	201.674945	−43.12846	1800.0	1780.0	1800.0	32.0	34.9	13.5
K-029	201.287304	−42.98286	1800.0	1780.0	1800.0	17.6	24.1	11.5
K-034	201.293745	−42.89216	1800.0	1780.0	1800.0	20.4	26.2	12.5
K-163	201.416752	−43.08328	1800.0	1780.0	1800.0	27.2	31.6	14.2
VHH81-03	201.241579	−42.93562	1800.0	1780.0	1800.0	18.8	24.7	13.9
VHH81-05	201.316943	−42.88218	1800.0	1780.0	1800.0	20.6	22.0	7.5

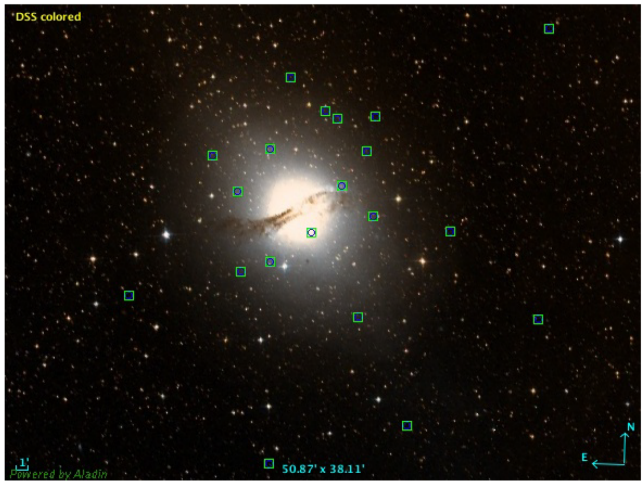

Figure 2. Colour composite image from the DSS2 optical HEALPIX survey, including ∼0.6 and ∼0.4 μm bands. Green squares locate the clusters studied as part of this work.

3 ABUNDANCE ANALYSIS

In this work, we make use of the integrated-light analysis tool developed and tested by L12. The L12 technique was originally created for high-dispersion observations of GCs, however in Hernandez et al. (2017), we showed that this method can also be used for detailed abundance analysis of intermediate-resolution observations. The original method is described in detail in the work of Larsen et al. (2012, 2014). The main idea involves an iterative process where the chemical abundances are determined by fitting synthetic modelled spectra to the integrated-light observations, varying the abundances on each iteration. To accurately model the observations one needs to account for every evolutionary stage present in the star cluster in question. We compute a single model atmosphere, which is then used to generate a high-resolution ($R \sim 500\,000$) synthetic spectrum for each stellar type. The individual model spectra are then combined on to a single synthetic integrated-light spectrum. We note that when co-adding the spectra we use appropriate weights accounting for the number of stars of a specific type based on a Salpeter IMF (see Section 3.1 for a detailed description). The synthetic integrated-light spectra are smoothed to match the resolution of the X-Shooter observations, and then compared to the science data.

In the original work of L12, the software made use of ATLAS9 models along with SYNTHE codes to compute the model atmospheres and synthetic spectra (Kurucz 1970; Kurucz & Furenlid 1979; Kurucz & Avret 1981). ATLAS9 is a 1D plane-parallel local thermodynamic equilibrium (LTE) atmospheric modelling software by Robert Kurucz. However, these plane-parallel models are less ideal for cooler stars. In our analysis in addition to using ATLAS9 and SYNTHE codes, we also use MARCS atmospheric models (Gustafsson et al. 2008) paired with TURBOSPECTRUM to create the synthetic spectra (Plez 2012). In contrast to ATLAS9, MARCS are 1D spherical LTE models. We download a grid of pre-computed MARCS models from their official website,[1] and allow the code to select the closest model to match the different stellar types. We use ATLAS9/SYNTHE software for stars with $T_{\rm eff} > 5000$K and MARCS/TURBOSPECTRUM for stars with $T_{\rm eff} < 5000$K, similar to what was done in Hernandez et al. (2018). Our analysis is based on the Solar composition from Grevesse & Sauval (1998).

The abundance analysis done in this paper is entirely based on LTE modelling. We note that we do not apply any non-LTE (NLTE) corrections as these are rather complex for integrated-light work given their dependence on the stellar properties of individual stars. In general NLTE corrections for some α-elements are predicted to range between −0.4 and −0.1 dex (Bergemann et al. 2015).

3.1 Theoretical+empirical stellar parameters

The distance to NGC 5128 makes obtaining colour–magnitude diagrams (CMDs) a complicated task. Given that CMDs for our star-cluster sample are not available, we instead rely on theoretical

[1] http://marcs.astro.uu.se

Table 2. Star-cluster properties from the literature.

Cluster	Age[a] (Gyr)	[m/H][a] (dex)	v_{rv}[b] (km s^{-1})	σ_{1D}[c] (km s^{-1})	Empirical HB and AGB[d]
AAT117062	10.00	−1.10	412 ± 71	–	NGC 0362
HGHH-04	10.00	−1.63	724 ± 46	14.0 ± 0.46	NGC 6093
HGHH-06	10.00	−1.10	790 ± 44	–	NGC 0362
HGHH-07	11.89	−1.03	593 ± 51	–	NGC 0362
HGHH-11	8.41	−0.43	721 ± 35	16.7 ± 1.5	NGC 6838
HGHH-17	10.00	−0.98	773 ± 46	20.8 ± 2.9	NGC 0362
HGHH-21	11.22	−1.10	495 ± 38	20.0 ± 1.4	NGC 0362
HGHH-23	10.59	−0.48	684 ± 24	41.5 ± 3.7	NGC 6838
HGHH-29	11.22	−0.45	743 ± 34	17.6 ± 1.8	NGC 6838
HGHH-34	8.41	−0.45	676 ± 27	–	NGC 6838
HGHH-40	10.00	−1.25	443 ± 48	–	NGC 0362
HH-080	10.00	−1.58	497 ± 33	–	NGC 6093
HH-096	10.00	−1.38	541 ± 54	–	NGC 0362
HHH86-30	5.01	−0.38	811 ± 32	–	Palomar 1
HHH86-39	11.89	−0.48	464 ± 42	–	NGC 0362
K-029	11.89	−0.75	249 ± 59	–	NGC 0104
K-034	11.22	−0.53	677 ± 44	–	NGC 0104
K-163	11.89	−0.98	487 ± 51	–	NGC 0362
VHH81-03	5.31	−0.20	591 ± 37	–	Palomar 1
VHH81-05	10.00	−1.55	563 ± 41	–	NGC 6093

Notes. [a]SSP ages and metallicities from Beasley et al. (2008).
[b]Values extracted from the work of Beasley et al. (2008).
[c]Line-of-sight velocity dispersion from Taylor et al. (2010) and Colucci et al. (2013).
[d]Galactic GC observations by Sarajedini et al. (2007) used to represent the HB and AGB stellar stages.

isochrones for the analysis. The selection of the atmospheric models is based on the theoretical α-enhanced isochrones by the Dartmouth group (Dotter et al. 2007) which account for main sequence and red giant branch (RGB) stars. We note that these isochrones exclude both, the horizontal branch (HB) and asymptotic giant branch (AGB) stages. For this reason, we opt for combining the theoretical isochrones with empirical HB and AGB observations from the survey of Galactic GCs using the Advanced Camera for Surveys on board the *Hubble Space Telescope* by Sarajedini et al. (2007).

For the initial selection of isochrones and appropriate empirical HB and AGB data, we adopt the ages and metallicities from Beasley et al. (2008) listed in Table 2. We extract the stellar parameters from the individual isochrones assuming an IMF following a power law with a Salpeter (1955) exponent, $\alpha = -2.35$. We adopt the luminosity limit of L12 where we only include stars brighter than $M_V = +9$. L12 points out that including stars fainter than this limit modifies the overall metallicities by <0.1 dex.

We also choose a CMD with similar age and metallicity as the ones listed in Table 2 and extract the photometry for stars in the HB and the AGB. For each of the GCs in NGC 5128, we list the Galactic GC used to model the HB and AGB populations in the last column of Table 2. The photometry is corrected for foreground extinction using the colour excess values, $E(B-V)$, from the latest edition of the Harris (1996) catalogue (version 2010). Most of the distance estimates used in the photometry come from the work of the 2010 edition of Harris (1996) and van den Bosch et al. (2006). For the HB and AGB stars, we derive values for the $T_{\rm eff}$ and bolometric corrections from the $V-I$ colours using the colour–$T_{\rm eff}$ transformation based on models by Kurucz (Castelli, Gratton & Kurucz 1997). Additionally, the surface gravities, $\log g$, are inferred using the relation

$$\log g = \log g_{\odot} + \log \left[\left(\frac{T_{\rm eff}}{T_{\rm eff\odot}} \right)^4 \left(\frac{M}{M_{\odot}} \right) \left(\frac{L_{\rm bol}}{L_{\rm bol\odot}} \right)^{-1} \right] \quad (1)$$

When combining the isochrone-based CMDs with the empirical HB and AGB data, similar to the approach of Larsen et al. (2017), we estimate the weights of the empirical data by matching the number of RGB stars in the range of $1 < M_V < 2$ in the theoretical CMD to those present in the empirical CMD.

We also account for the microturbulent velocity component, v_t, assigning different values depending on their $\log g$. For stars with $\log g > 4.5$, we adopt a value of $v_t = 0.5$ km s^{-1} (Takeda et al. 2002). Following the reference points of L12 and Larsen et al. (2017), for $4.0 < \log g < 4.5$, we assume $v_t = 1.0$ km s^{-1} and for $\log g < 1.0$, $v_t = 2.0$ km s^{-1}. For values $1.0 < \log g < 4.0$, we assign microturbulent velocities based on a linear interpolation of $v_t(\log g)$. Lastly, for HB stars, we assume $v_t = 1.8$ km s^{-1} (Pilachowski, Sneden & Kraft 1996).

3.2 Smoothing parameter

After the synthetic integrated-light spectrum is produced, we degrade the resolution of the model spectrum from $R = 500\,000$ to $R \sim 6200$–$11\,000$ to match the X-Shooter observations. In our analysis, we are able to fit for the best Gaussian dispersion, $\sigma_{\rm sm}$, which should account for the instrumental resolution ($\sigma_{\rm inst}$) and the cluster velocity dispersion ($\sigma_{\rm 1D}$).

As a first step in this analysis, we fit for the radial velocities ($v_{\rm rv}$) and the best $\sigma_{\rm sm}$ along with the overall metallicity, [Z], processing 200 Å of data at a time. Given that X-Shooter collects data through a multiple-arm system detailed in Section 2, we fit separate $\sigma_{\rm sm}$ for each arm. We scan the UVB wavelength range between 4000 and 5200 Å, and for the VIS arm we use the spectroscopic observations covering wavelengths between 6100 and 8850 Å excluding areas affected by strong telluric absorption.

Using slit widths of 0.5 arcsec for the UVB arm and 0.7 arcsec for the VIS arm, Chen et al. (2014) find that the instrumental resolution in the UVB arm varies between $R = 9584$ and 7033. In contrast to

Table 3. Derived velocities.

Cluster	v_{rv} (km s^{-1})	σ_{1D} (km s^{-1})
AAT117062	495 ± 4	20.2 ± 4.4
HGHH-04	699 ± 4	15.7 ± 8.5
HGHH-06	845 ± 3	28.5 ± 3.7
HGHH-07	589 ± 3	24.7 ± 2.5
HGHH-11	750 ± 3	16.6 ± 2.4
HGHH-17	777 ± 2	19.0 ± 1.6
HGHH-21	457 ± 3	17.1 ± 2.5
HGHH-23	672 ± 1	29.2 ± 3.0
HGHH-29	721 ± 3	14.7 ± 1.7
HGHH-34	638 ± 4	10.8 ± 2.8
HGHH-40	372 ± 3	4.7 ± 5.1
HH-080	470 ± 3	12.4 ± 4.0
HH-096	610 ± 3	13.6 ± 5.0
HHH86-30	768 ± 3	22.3 ± 1.7
HHH86-39	227 ± 5	12.5 ± 2.2
K-029	629 ± 3	25.3 ± 1.1
K-034	452 ± 2	14.4 ± 2.1
K-163	477 ± 3	22.2 ± 1.3
VHH81-03	553 ± 1	17.5 ± 2.4
VHH81-05	555 ± 3	10.2 ± 5.3

their findings regarding the UVB observations, the VIS arm showed a constant resolution throughout the wavelength coverage with an average value of $R = 10\,986$, very similar to the X-Shooter stated resolution of $R = 11\,000$.[2] Following the results of Chen et al. (2014), we assume that the resolving power follows a Gaussian full width half-maximum, and a constant resolution in the VIS arm with a value of $R = 11\,000$, corresponding to an instrumental velocity dispersion of $\sigma_{inst} = 11.58\,km\,s^{-1}$.

We estimate the line-of-sight velocity dispersions by subtracting σ_{inst} in quadrature from the averaged σ_{sm} for the VIS data. We note that the work presented here assumes an instrumental resolution set by the configuration alone, i.e. slit width. In Table 3, we list our inferred radial velocity and the line-of-sight velocity dispersions for each of the clusters in the sample.

For completeness, in Fig. 3, we compare our inferred velocities, both radial velocity and line-of-sight velocity dispersion, to values in the literature listed in Table 2. The left-hand panel of Fig. 3 shows excellent agreement between our measured radial velocities with those from the work of Beasley et al. (2008) for all 20 GCs. We note that the errors in the radial velocity measurements are determined from the scatter around the mean value, using the standard deviation of the measurements.

In the right-hand panel of Fig. 3, we plot our inferred velocity dispersions against those from the work of Taylor et al. (2010) and Colucci et al. (2013). Unfortunately, literature measurements of σ_{1D} are more limited than v_{rv}. Taylor et al. (2010) measured σ_{1D} for seven GCs in our sample. We find good agreement for all but one GC, HGHH-23, where Taylor et al. (2010) find a significantly higher velocity dispersion. Our value for HGHH-23, however, is in good agreement with that inferred by Rejkuba et al. (2007), $\sigma_{1D} = 30.5 \pm 0.2\,km\,s^{-1}$, well within the errors of our measured velocity dispersion of $\sigma_{1D} = 29.2 \pm 3.0\,km\,s^{-1}$.

We point out that although our measurements for σ_{1D} agree well with values in the literature, some of our inferred velocity dispersions are relatively high, when compared to the standard σ_{1D} measured for Galactic GCs. From the latest edition of the Harris (1996) catalogue (version 2010), we see that the highest σ_{1D} values measured in Galactic GCs are around $\sim$18 km s^{-1}. The velocity dispersion values measured for GCs in NGC 5128 range between $5 \lesssim \sigma_{1D} \lesssim 30\,km\,s^{-1}$. That being said, we note that the GC system in NGC 5128 is rich and remarkably larger than that of the MW, and in this study, we are probing the brightest GCs in NGC 5128, which could in principle mean that we are looking at the most massive GCs in this early-type galaxy.

3.3 Element spectral windows

As detailed in Hernandez et al. (2017), one of the main challenges in working with integrated-light observations of star clusters is the degree of blending suffered by the different spectral lines. In Hernandez et al. (2017), we created optimized spectral windows tailored for individual elements. The windows were carefully selected to mitigate strong blending based on a series of criteria. For a more detailed discussion of the optimization of the spectral windows, we refer the reader to Hernandez et al. (2017, Section 3.4). Briefly, we create two synthetic spectra using the physical parameters of Arcturus as published by Ramírez & Allende (2011). One of the spectra is generated excluding all lines for the element in question, whereas the second spectrum includes *only* spectral features for the same element under analysis. Comparing the two spectra, we make a pre-selection of spectral lines with a minimal degree of blending based on the following requirements: (i) from the normalized spectra the depth of the spectral absorption must have a maximum flux of 0.85, and (ii) neighbouring lines closer than ±0.25 Å are excluded. This pre-selection is done automatically using a PYTHON script. We continue to inspect the recommended element lines and finalize the wavelength windows which include the majority of the clean lines. We note that for Fe and Ti, we select broader windows as most of the wavelength range is populated by spectral lines of these elements.

4 RESULTS

After correcting for the radial velocities, and once the smoothing parameter (σ_{sm}) has been inferred, we fit for the overall metallicity, [*Z*], keeping σ_{sm} fixed. This exercise is performed on each cluster analysing the data in 200 Å intervals. These initial metallicities are only used as a first step, mainly as a scaling factor, before proceeding to measure the individual elements. For wavelength windows of ≥100 Å, we match the continua of the model spectra with those of the observations using a cubic spline with three knots. For spectral windows of <100 Å, we instead use a first-order polynomial to fit the continuum. We initiate the detailed abundance analysis, first measuring Fe. We start with those elements with the highest number of lines throughout the spectral coverage. For this element, we again scan the wavelength range analysing 200 Å at a time, covering wavelengths between 4400 and 8850 Å excluding the noisy arm edges and telluric contaminated regions. In general, we find consistent results throughout the different bins. In Fig. 4, we show the individual Fe abundances for the corresponding wavelength bins for a selected sample. We do not observe any strong trends with wavelength. Additionally, for this same selected sample of GCs, in Figs A1–A5, we present element abundances as a function of their corresponding wavelength bin.

We continue down the element list measuring Ti, Ca, Mg, Cr, Mn, Ni, and Na, one element at a time. We point out that the L12 code allows for fittings that include multiple elements simultaneously;

[2] https://www.eso.org/sci/facilities/paranal/instruments/xshooter/inst.html

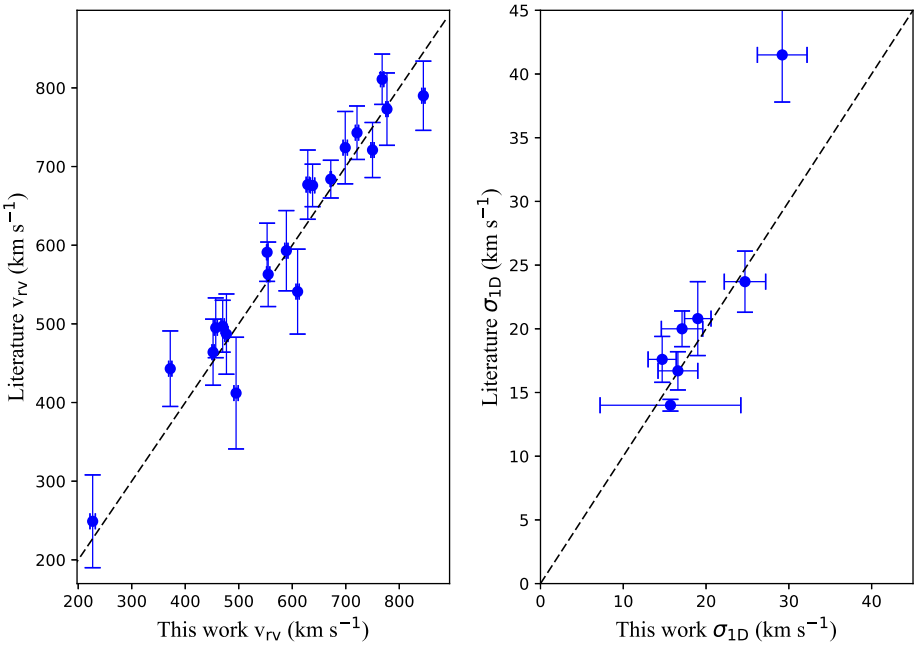

Figure 3. Left-hand panel: comparison between radial velocities (v_{rv}) measured in this work and in Beasley et al. (2008). Right-hand panel: comparison between line-of-sight velocity dispersions inferred in this work and those in the work of Taylor et al. (2010) and Colucci et al. (2013). Dashed lines show the line of equal value.

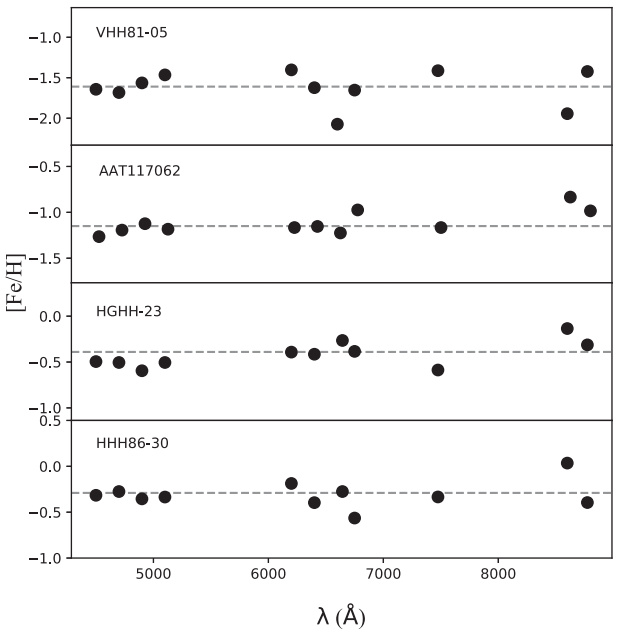

Figure 4. Fe abundances as a function of wavelength for a selected sample of GCs in NGC 5128. The grey dashed line shows the inferred [Fe/H] for the corresponding clusters. We present the clusters from top to bottom in order of increasing metallicity.

however, fitting individual elements appears to be slightly more efficient. For each element, we use the tailored wavelength windows optimized following the criteria presented in Section 3.3. As we proceed with the analysis, we keep the measured abundances fixed to their best-fitting value, and continue with the rest of the elements. In Tables A1–A20, we show the elements, wavelength bins, best-fitting abundances, and their respective 1σ uncertainties from the χ^2 fit. Additionally, in Fig. 5, we show normalized synthesis fits for a selected star-cluster sample covering wavelengths 5000–5200 Å.

In Tables 4 and 5, we present our final abundances, along with their corresponding errors, σ_X. The values in these tables are estimates of the weighted average abundances. When calculating these values we assume weights defined as $w_i = 1/\sigma_i^2$, where σ_i represents the 1σ errors listed in Tables A1–A20. Given that the scatter in the individual measurements is larger than the errors based on the χ^2 fits, we believe that the standard deviation, σ_{STD}, appears to be more representative of the actual uncertainties. Therefore, we turn the σ_{STD} into formal errors of the mean abundances following:

$$\sigma_X = \frac{\sigma_{STD}}{\sqrt{N-1}} \quad (2)$$

In equation (2), σ_{STD} and N represent the standard deviation and number of bins for the elements in question, respectively.

4.1 Sensitivity to input isochrones

The integrated-light analysis done here relies on theoretical models. We make use of α-enhanced isochrones by the Dartmouth group, as we are mainly studying relatively older populations. However, to test the uncertainties involved in a particular choice of theoretical isochrones, we repeat the full abundance analysis using instead solar-scaled Padova and Trieste Stellar Evolution Code (PARSEC) isochrones (Bressan et al. 2012). An additional difference between the α-enhanced Dartmouth isochrones and the solar-scaled PARSEC models, other than the chemical composition, is the stellar evolutionary phase coverage. The PARSEC models include the HB and AGB phases and do not require empirical data for the post-RGB stellar phases.

In Fig. 6, we compare [Fe/H] as measured using α-enhanced isochrones (Dartmouth) and solar-scaled isochrones (PARSEC). We find that the average difference is $\lesssim$0.1 dex. The highest difference is observed in the most metal-rich GC, VHH81-03, with a difference in

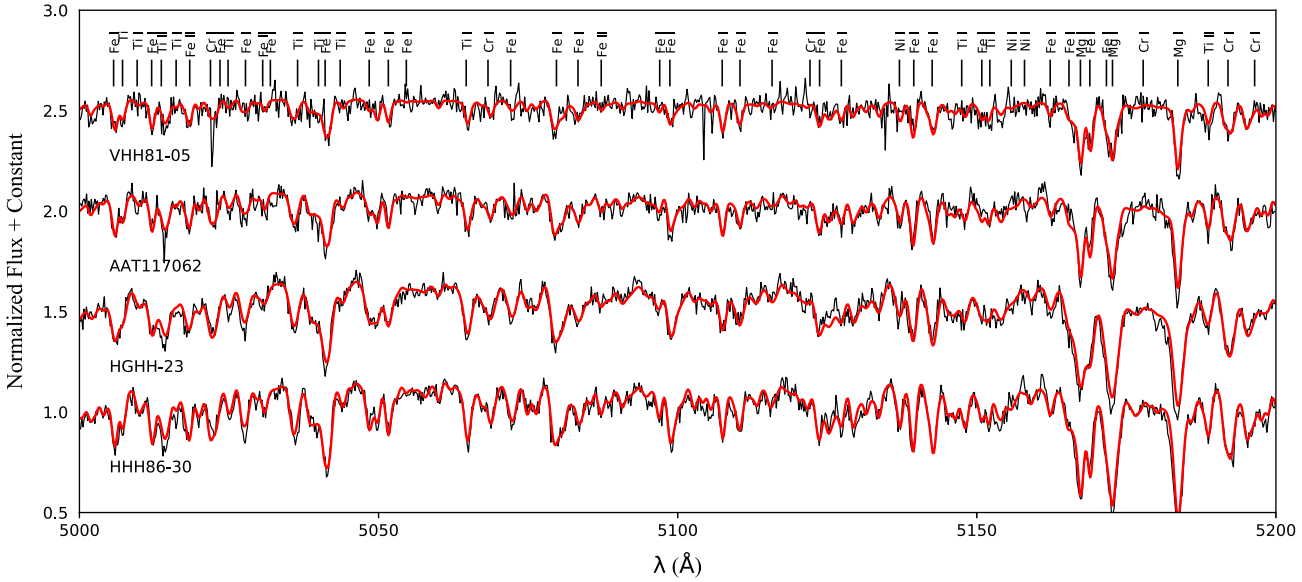

Figure 5. Normalized synthesis fits for a selected sample of GCs in NGC 5128. In black, we show the X-Shooter observations. In red, we show the model fit. The individual cluster names are located below the corresponding spectra. We present the clusters from top to bottom in order of increasing metallicity given our results.

Table 4. Derived metallicities.

Cluster	[Fe/H] $\pm \sigma_{\rm Fe}$ (dex)
AAT117062	-1.15 ± 0.04
HGHH-04	-1.92 ± 0.06
HGHH-06	-0.92 ± 0.02
HGHH-07	-1.13 ± 0.03
HGHH-11	-0.47 ± 0.05
HGHH-17	-1.09 ± 0.03
HGHH-21	-0.96 ± 0.04
HGHH-23	-0.39 ± 0.04
HGHH-29	-0.51 ± 0.03
HGHH-34	-0.40 ± 0.03
HGHH-40	-1.13 ± 0.04
HH-080	-1.62 ± 0.07
HH-096	-1.29 ± 0.05
HHH86-30	-0.29 ± 0.04
HHH86-39	-1.25 ± 0.08
K-029	-0.74 ± 0.02
K-034	-0.52 ± 0.03
K-163	-1.10 ± 0.04
VHH81-03	-0.13 ± 0.05
VHH81-05	-1.61 ± 0.07

the estimated [Fe/H] of ∼0.2 dex. From Fig. 6, we can see that at low metallicities ([Fe/H] < -1.0), the inferred [Fe/H] abundances agree with each other. Larsen et al. (2017) compared metallicities obtained from integrated-light observations for seven Galactic GCs using Dartmouth isochrones and MIST (MESA Isochrones and Stellar Tracks, Choi et al. 2016; Dotter 2016) models. Their sample spanned metallicities from [Fe/H] ~ -2.4 to ~ -0.5 dex. Similar to our test results, Larsen et al. (2017) found comparable metallicities and abundances for the most metal-poor clusters, [Fe/H] < -2.0 using both models, Dartmouth and MIST. The metal-rich regime appeared to have larger model dependencies than what was observed for the metal-poor end. Similar results were observed by Colucci et al. (2016) when comparing their Galactic GC [Fe/H] derived from integrated-light observations and those from Harris (1991, 2010 edition). They find accurate values to within ∼0.1 dex at low metallicities, [Fe/H] $\lesssim -0.3$ dex, and observe higher offsets for the metal-rich clusters. This might be caused by the similarities between different theoretical isochrones, especially in what appears to be the better understood metal-poor regime. In general, it seems that Fe abundances from integrated-light analysis are more robust at lower metallicities, than at higher values ([Fe/H] > -1.0 dex).

In the different panels of Fig. 7, we compare the abundances obtained for the rest of the elements. Replacing the α-enhanced isochrones with solar-scaled models increases the [Mg/Fe] abundances on average by ∼0.12 dex. For [Ca/Fe] ratios, the differences between the two runs are comparatively smaller, with average differences of the order of 0.05 dex (top right panel in Fig. 7). Changing the isochrone models from α-enhanced to solar-scaled decreases the [Ti/Fe] ratios only slightly, with average differences of ∼0.08 dex. Overall, we find no correlation between the differences in the abundance ratios of [(Ca, Ti)/Fe] and the [Fe/H] abundances. For Mg, however, we see a slight correlation where the largest differences are seen in the two clusters with higher metallicities, VHH81-03 and HHH86-30.

In addition to the α-elements, we also estimate abundances for Fe-peak elements changing the input models. The average differences for [Cr/Fe], [Mn/Fe], and [Ni/Fe] ratios is ∼0.05, 0.08, and 0.05, respectively. Comparison abundances for Fe-peak elements are also shown in Fig. 7. No general correlations between the ratio differences and metallicity are observed for any of the Fe-peak elements.

4.2 Fe and Ca abundances: comparison with literature

Beasley et al. (2008) derived empirical metallicities, [m/H], for all 20 GCs in our sample. In the left-hand panel of Fig. 8 (red circles), we compare our metallicities to those measured by Beasley et al. (2008). In general, we find excellent agreement between their work, and our inferred [Fe/H] abundances, except for GC HHH86-39. For this cluster, Beasley et al. estimate a metallicity of [m/H] $= -0.48$,

Table 5. Derived abundances.

Cluster	[Mg/Fe] $\pm\sigma_{\rm Mg}$ (dex)	[Ca/Fe] $\pm\sigma_{\rm Ca}$ (dex)	[Ti/Fe] $\pm\sigma_{\rm Ti}$ (dex)	[Na/Fe] $\pm\sigma_{\rm Na}$ (dex)	[Cr/Fe] $\pm\sigma_{\rm Cr}$ (dex)	[Mn/Fe] $\pm\sigma_{\rm Mn}$ (dex)	[Ni/Fe] $\pm\sigma_{\rm Ni}$ (dex)
AAT117062	$+0.55 \pm 0.13$	$+0.25 \pm 0.10$	$+0.39 \pm 0.14$	–	$+0.11 \pm 0.20$	-0.08 ± 0.24	$+0.17 \pm 0.07$
HGHH-04	$+0.44 \pm 0.17$	$+0.53 \pm 0.16$	$+0.51 \pm 0.10$	–	$+0.12 \pm 0.20$	-0.70 ± 0.29	$+0.04 \pm 0.11$
HGHH-06	$+0.64 \pm 0.06$	$+0.33 \pm 0.16$	$+0.33 \pm 0.10$	–	$+0.16 \pm 0.13$	-0.25 ± 0.29	$+0.24 \pm 0.15$
HGHH-07	$+0.53 \pm 0.13$	$+0.48 \pm 0.13$	$+0.28 \pm 0.10$	$+0.26 \pm 0.20$	$+0.08 \pm 0.19$	-0.05 ± 0.28	$+0.13 \pm 0.08$
HGHH-11	$+0.32 \pm 0.11$	-0.09 ± 0.12	$+0.13 \pm 0.15$	$+0.04 \pm 0.08$	-0.12 ± 0.08	$+0.25 \pm 0.29$	$+0.08 \pm 0.11$
HGHH-17	$+0.52 \pm 0.10$	$+0.44 \pm 0.08$	$+0.27 \pm 0.05$	$+0.04 \pm 0.18$	$+0.17 \pm 0.30$	-0.02 ± 0.17	$+0.15 \pm 0.07$
HGHH-21	$+0.54 \pm 0.09$	$+0.31 \pm 0.09$	$+0.43 \pm 0.11$	–	$+0.20 \pm 0.24$	$+0.17 \pm 0.07$	$+0.24 \pm 0.19$
HGHH-23	$+0.28 \pm 0.14$	$+0.01 \pm 0.11$	$+0.05 \pm 0.23$	$+0.38 \pm 0.08$	$+0.09 \pm 0.19$	$+0.13 \pm 0.29$	-0.12 ± 0.18
HGHH-29	$+0.43 \pm 0.06$	$+0.04 \pm 0.06$	$+0.28 \pm 0.07$	–	$+0.26 \pm 0.29$	$+0.20 \pm 0.23$	$+0.12 \pm 0.14$
HGHH-34	$+0.35 \pm 0.09$	$+0.00 \pm 0.06$	$+0.49 \pm 0.18$	–	$+0.02 \pm 0.18$	$+0.18 \pm 0.06$	$+0.23 \pm 0.10$
HGHH-40	$+0.24 \pm 0.09$	$+0.19 \pm 0.07$	$+0.27 \pm 0.25$	–	$+0.05 \pm 0.44$	-0.13 ± 0.06	$+0.30 \pm 0.32$
HH-080	$+0.18 \pm 0.14$	$+0.35 \pm 0.09$	$+0.30 \pm 0.14$	–	$+0.04 \pm 0.19$	-0.01 ± 0.18	$+0.03 \pm 0.14$
HH-096	$+0.35 \pm 0.22$	$+0.38 \pm 0.05$	$+0.27 \pm 0.07$	–	$+0.09 \pm 0.12$	-0.24 ± 0.22	$+0.14 \pm 0.10$
HHH86-30	$+0.29 \pm 0.06$	-0.19 ± 0.13	$+0.27 \pm 0.12$	$+0.26 \pm 0.10$	$+0.25 \pm 0.17$	$+0.18 \pm 0.08$	$+0.10 \pm 0.07$
HHH86-39	–	$+0.12 \pm 0.20$	$+0.24 \pm 0.25$	-0.05 ± 0.11	$+0.13 \pm 0.63$	-0.32 ± 0.26	-0.13 ± 0.15
K-029	$+0.44 \pm 0.11$	$+0.16 \pm 0.14$	$+0.22 \pm 0.12$	$+0.70 \pm 0.08$	$+0.15 \pm 0.25$	$+0.11 \pm 0.50$	$+0.00 \pm 0.11$
K-034	$+0.42 \pm 0.12$	-0.01 ± 0.08	$+0.21 \pm 0.06$	$+0.34 \pm 0.08$	$+0.25 \pm 0.19$	$+0.14 \pm 0.03$	$+0.09 \pm 0.11$
K-163	$+0.60 \pm 0.13$	$+0.43 \pm 0.09$	$+0.28 \pm 0.06$	$+0.65 \pm 0.22$	$+0.02 \pm 0.19$	-0.21 ± 0.17	$+0.09 \pm 0.13$
VHH81-03	$+0.22 \pm 0.08$	-0.17 ± 0.16	$+0.12 \pm 0.10$	–	$+0.14 \pm 0.29$	$+0.21 \pm 0.29$	$+0.10 \pm 0.10$
VHH81-05	$+0.25 \pm 0.12$	$+0.54 \pm 0.09$	$+0.55 \pm 0.17$	–	-0.11 ± 0.61	-0.19 ± 0.06	-0.40 ± 0.11

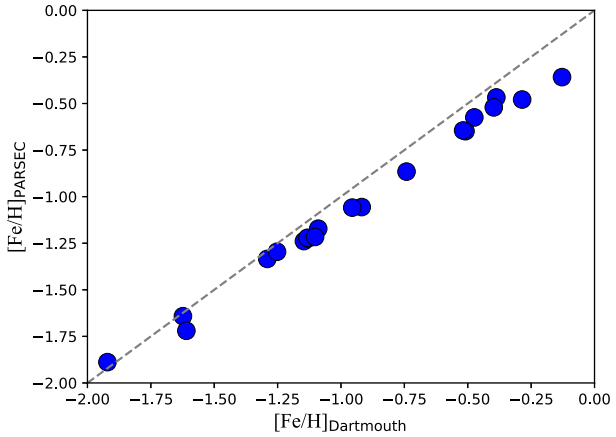

Figure 6. Comparison between the metallicities inferred using α-enhanced isochrone (Dartmouth), and solar-scaled isochrones (PARSEC). The grey dashed line shows equal values.

whereas we find an [Fe/H] abundance of -1.29 ± 0.05 dex. As described in Section 3.1 for the initial selection of isochrones and empirical CMDs, we adopt the ages and metallicities by Beasley et al. (2008). For HHH86-39, we initially select an isochrone with metallicity -0.48 dex, and see that the inferred metallicities converge on to lower values. We continue re-estimating the metallicity for HHH86-39 using instead an isochrone with [Fe/H] $= -1.28$ dex and estimate a consistent [Fe/H] abundance of -1.29 ± 0.05. Given the self-consistency between the input isochrone and the measured [Fe/H] abundance, we continue our analysis adopting the inferred [Fe/H] $= -1.29 \pm 0.05$ dex. As we noted earlier, the line index techniques used by Beasley et al. (2008) do not measure [Fe/H] necessarily. However, an overall metallicity comparison is still a useful test.

Using high-resolution and high S/N integrated-light observations Colucci et al. (2013) measured Fe and Ca abundances for a sample of 10 GCs in NGC 5128. Of the 10 clusters in Colucci et al. (2013), we have four clusters in common between their study and our work.

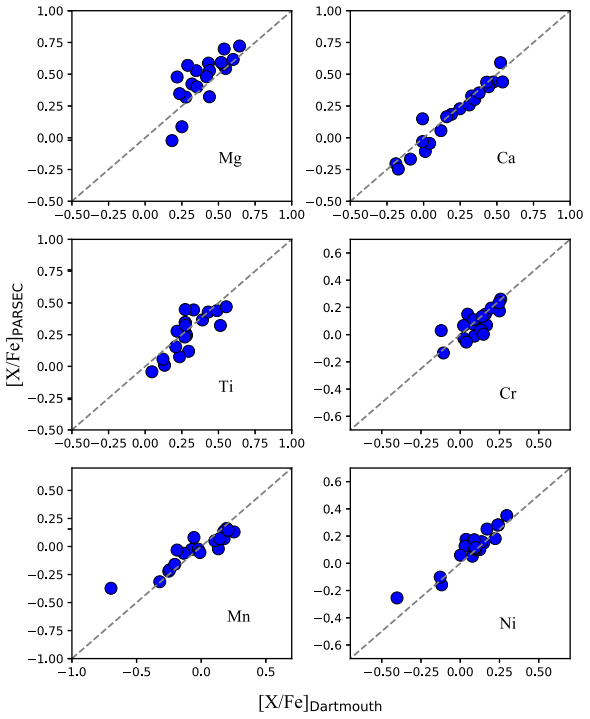

Figure 7. Comparison between the detailed abundances measured using α-enhanced isochrone (Dartmouth), and solar-scaled isochrones (PARSEC). The element in question is indicated in the corresponding panel. The grey dashed line shows equal values.

From a direct comparison to the metallicities obtained by Colucci et al. (2013), we see an average offset of $\sim +0.2$ dex between their metallicities and those estimated here; however, they all agree within 2σ (see Fig. 8, left-hand panel).

Similarly, in the right-hand panel of Fig. 8, we compare our inferred [Ca/Fe] ratios to those obtained by Colucci et al. (2013). The [Ca/Fe] ratios of three out of four clusters are in excellent agreement, within 1σ, to those measured in the high-resolution

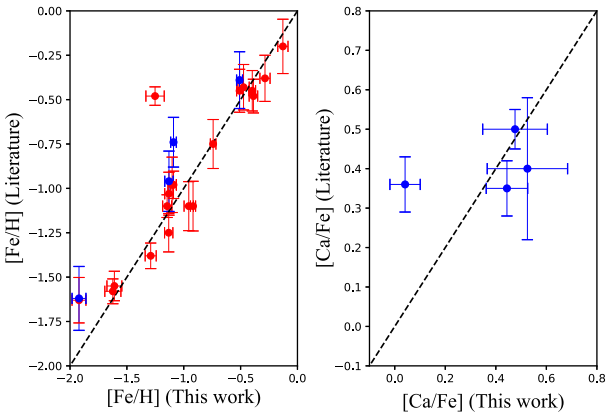

Figure 8. [Fe/H] and [Ca/Fe] abundance comparison between this work and that from Colucci et al. 2013 (in blue circles), and Beasley et al. 2008 (in red circles). The dash line in both panels represents a 1:1 relation.

observations. The Ca abundance for the fourth cluster, HGHH-29, appears to be a 3σ outlier compared to our [Ca/Fe] measurements with an offset of the order of $\sim$0.3 dex. We visually inspect the Ca model fits and find no anomalies, as well as consistent [Ca/Fe] abundances between the different bins.

5 DISCUSSION

In this section, we discuss our abundance measurements, along with a comparison to other NGC 5128 abundance studies in the literature. We also compare the abundance patterns observed in NGC 5128 to those studied in different environments, such as the MW and M 31.

5.1 α-elements

As mentioned before, it is believed that α-elements (O, Mg, Si, Ca, and Ti) are primarily produced in high-mass stars and ejected through core-collapse supernovae (Woosley & Weaver 1995). Given that these elements are believed to be part of a homogenous group, it is common for abundance studies to average their abundances to obtain a single [α/Fe] ratio. In general, the abundances of these different elements appear to correlate tightly with each other in Galactic stars. However, [Mg/Fe] has been observed to be slightly more enhanced than the rest of the α-elements in dSph galaxies (Shetrone 2004; Venn et al. 2004). This difference between the Mg ratios and those of Ca and Ti could have nucleosynthetic origins. Although all three elements, Mg, Ca, and Ti, are produced inside high-mass stars, Mg is created through hydrostatic C- and O-burning, in contrast to Ca and Ti isotopes which are formed in the α-process (Woosley & Weaver 1995; Nakamura et al. 2001). If these two processes do not occur together, then one would expect to see differences in the [Mg/Fe] ratios when compared to those of [Ca/Fe] and [Ti/Fe]. This being said, the differences in the [Mg/Fe] and [(Ca,Ti)/Fe] ratios might also be explained by different star formation histories, mixing time-scales or IMFs.

In Fig. 9, we display the [Mg/Fe], [Ca/Fe], and [Ti/Fe] ratios as a function of metallicity for all 20 GCs in NGC 5128 (red stars). We compare our NGC 5128 α-element abundances to those observed in Galactic stars for both halo and disc stars (black crosses), MW bulge stars (yellow points), and GCs in the MW (green circles). We also include the [Ca/Fe] abundances for the GC sample in NGC 5128 studied by Colucci et al. (2013) as blue stars. It is important to note that the MW stellar abundances shown as black crosses in Fig. 9 cover the different Galactic components, halo, thin and thick discs. An analysis focused on the kinematical information available for different MW stars allowed Venn et al. (2004) to assign stars to different Galactic components finding that halo stars reach metallicities as high as [Fe/H] ~ -1 dex. At higher metallicities than this MW disc stars seem to predominate. As seen from Fig. 9, all of the star clusters in our sample of NGC 5128 with [Fe/H] < -0.5 dex are enhanced in [α/Fe] relative to solar abundance.

It is clear from the top panel of Fig. 9 that we measure relatively high enhancement in [Mg/Fe] ratios, when compared to what is seen in the MW (GCs and field stars). For lower metallicities, [Fe/H] < -0.75 dex, we measure an average [Mg/Fe] $= +0.49 \pm 0.05$ for the GCs in NGC 5128, compared to [Mg/Fe] $= +0.33 \pm 0.01$ for Galactic stars (mainly halo stars), and [Mg/Fe] $= +0.33 \pm 0.03$ for GCs in the MW. We note that the errors are estimated by turning the standard deviation estimates into errors on the mean abundances. The highest enhancement in the [Mg/Fe] ratios is observed in six GCs with metallicities in the range of $-1.15 <$ [Fe/H] < -0.92 dex, with average [Mg/Fe] ~ 0.56 dex. If we instead compare the mean [Mg/Fe] ratios for GCs with metallicities [Fe/H] < -1.25 dex, we find [Mg/Fe] $= +0.31 \pm 0.06$ and $+0.32 \pm 0.04$ for GCs in NGC 5128 and the MW, respectively. To confirm if the enhancement at metallicities [Fe/H] < -0.75 dex is genuine, we recommend extending the GCs sample size in NGC 5128 to cover a larger range in metallicities, similar to the GC sample in the MW (with metallicities at the lower end extending to [Fe/H] ~ -2.4 dex). For metallicities higher than [Fe/H] > -0.75, the [Mg/Fe] ratios are close to the upper envelope of measurements of field stars in the MW (black crosses) and rather comparable to average [Mg/Fe] values found in Galactic bulge stars (yellow points). For comparison to the GCs in the MW, we take the weighted averages and find mean [Mg/Fe] ratios of $+0.34 \pm 0.03$ and $+0.24 \pm 0.13$ for the GCs in NGC 5128 and Galactic GCs, respectively, where we might be detecting a slightly higher enhancement in the NGC 5128 GCs compared to the few GCs in the MW at these metallicities.

For the Ca abundances in GCs in NGC 5128, Colucci et al. (2013) reported a relatively high enhancement of [Ca/Fe] $= +0.37 \pm 0.07$ for clusters with metallicities of [Fe/H] < -0.4. For consistency, we take the [Ca/Fe] ratios of Colucci et al. (2013) and calculate a simple mean for clusters with [Fe/H] < -0.75, which gives [Ca/Fe] $= +0.39 \pm 0.03$. Taking the mean of our inferred [Ca/Fe] for GCs with [Fe/H] < -0.75, we obtain [Ca/Fe] $= +0.36 \pm 0.04$, certainly within the errors of the mean abundance ratio of Colucci et al. (2013). Again, these values are higher than what is observed in the MW stars at the same metallicities, [Ca/Fe] $+0.27 \pm 0.01$. The agreement between the two independent studies of NGC 5128 confirms the Ca abundance enhancement in the metal-poor GCs. At metallicities [Fe/H] > -0.75, the [Ca/Fe] ratios decrease to solar/subsolar abundances, which is rarely observed in any of the MW components. The two most metal-rich GCs in our sample, HHH86-30 and VHH81-03, appear to be those with the lowest [Ca/Fe] abundance ratios. We note that abundances in the GC sample by Colucci et al. (2013) show instead a less steep decrease in [Ca/Fe] towards higher metallicities.

We also see enhanced Ti abundances with a mean value [Ti/Fe] $= +0.32 \pm 0.03$, for metallicities [Fe/H] < -0.75 (see bottom panel of Fig. 9). This in contrast to the mean [Ti/Fe] ratio seen in Galactic stars, [Ti/Fe] $= +0.25 \pm 0.01$, and a similar mean average for MW GCs, [Ti/Fe] $= +0.25 \pm 0.02$. Resembling what we observe in the [Mg/Fe] ratios at higher metallicities, [Fe/H] > -0.75, we find that the [Ti/Fe] abundances are more comparable to the few [Ti/Fe] ratios measured in the MW bulge, which tend to be on the upper

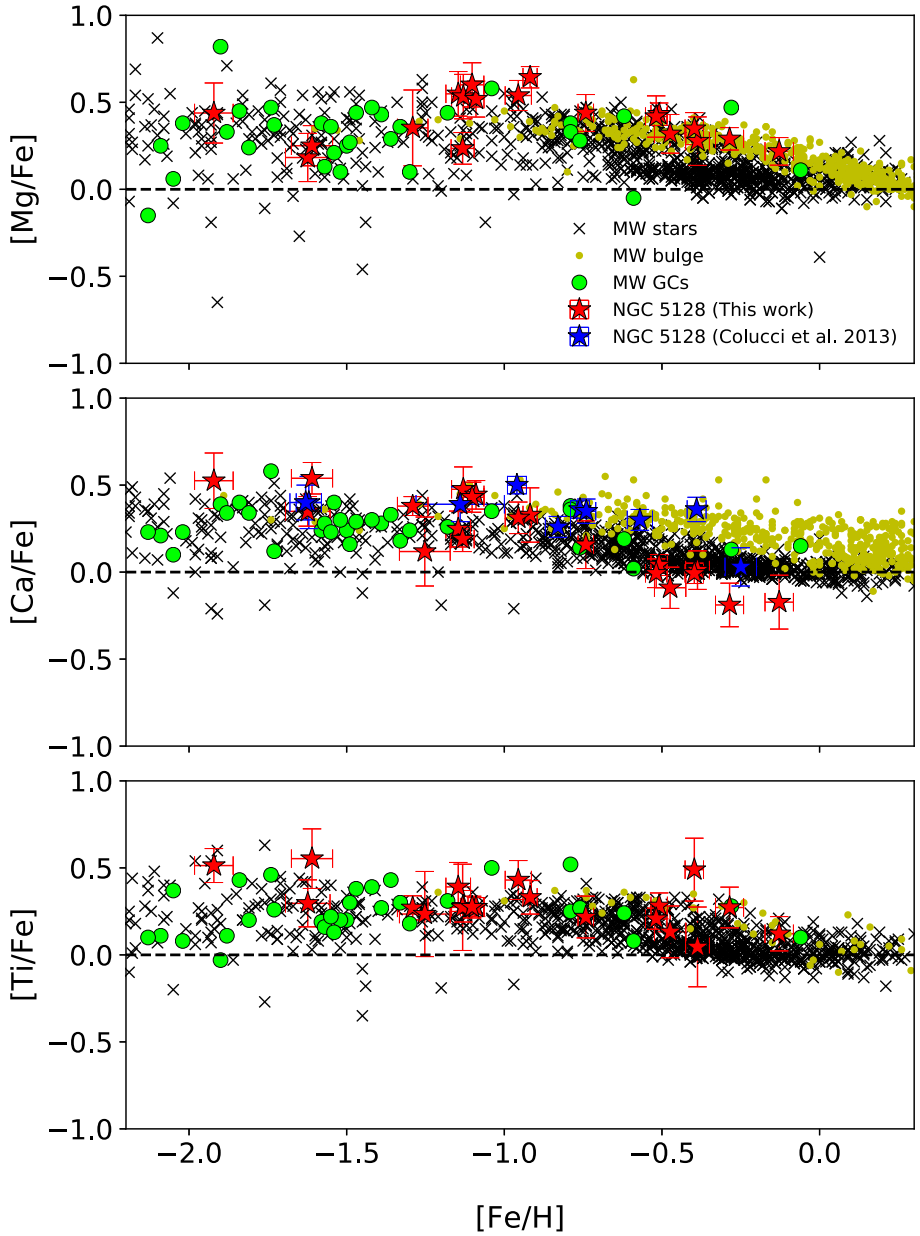

Figure 9. Top: [Mg/Fe] versus [Fe/H]. Middle: [Ca/Fe] versus [Fe/H]. Bottom: [Ti/Fe] versus [Fe/H]. In red stars, we show the α abundances for GCs in NGC 5128 (this work). Blue stars show the abundances for GCs in NGC 5128 by Colucci et al. (2013). Green circles show abundance measurements of GCs in the MW by Pritzl et al. (2005). Black crosses show the ratio abundance of MW stars found in the literature (Reddy et al. 2003, 2006; Venn et al. 2004; Ishigaki et al. 2013). Abundance measurements for bulge stars in the MW are shown in yellow points (Bensby et al. 2013; Johnson et al. 2014; Gonzalez et al. 2015).

envelope of the stellar abundances in the MW (black crosses in Fig. 9).

In general, the [α/Fe] abundances for GCs with [Fe/H] < -0.75 in NGC 5128 appear to be higher than those observed in the MW by $\sim$0.10–0.15 dex. We note that systematic differences between the measurement techniques cannot be ruled out as a possible cause for the observed enhancement of the [α/Fe] ratios. A broad range of studies infer different abundances provided the different methods, models, and parameters used. As discussed in Section 4.1, similar offsets are seen when changing the input isochrones from α-enhanced to solar-scaled for Mg abundances. However, the agreement between the Ca enhancement in the metal-poor GCs in the independent study by Colucci et al. (2013) and this work adds confidence to the validity of the measurements.

If the overall enhancement in the α-elements measured in this work is genuine, this could hint at an IMF skewed to high-mass stars. We also note that in addition to relatively high α abundances, through an empirical spectroscopic study of the metallicity distribution function of the GC system in NGC 5128 Beasley et al. (2008) find that the mean metallicity of this galaxy is $\sim$0.5 dex more metal rich than that of the MW GC system (Schiavon et al. 2005; Puzia et al. 2002). The combination of these two effects, high average metallicity and enhanced [α/Fe] ratios, might indicate that high-mass SNe II have been the main drivers in chemically diversifying the galaxy environment (McWilliam 1997). In a large study of metallicity and abundance ratios of early-type galaxies such as NGC 5128, using galaxy chemical evolution semi-analytical models (SAMs) with feedback from active galactic nuclei (AGNs) Arrigoni

et al. (2010) find that in order to reproduce the galaxy observations, more specifically the observed positive slope in the mass–[α/Fe] relation, they have to apply a mildly top-heavy IMF along with a lower fraction of binaries that explodes as SNe Ia. The original expectation of this work was that the inclusion of the AGN feedback in the simulations would be able to reproduce the observed trend in mass and [α/Fe] ratios. However, they point out that a flatter IMF (skewed to high-mass stars) is needed to achieve the best agreement between observations and model. A slightly top-heavy IMF produces more massive stars, which in turn enrich the interstellar medium more efficiently allowing for more metal-rich galaxies and a better agreement with observed abundances.

Similar high enhancements were found by Puzia, Kissler-Patig & Goudfrooij (2006) in a large number of GCs in early-type galaxies. In their study, they find significantly high [α/Fe] abundances derived from Lick line index measurements, of the order of [α/Fe] > 0.5 dex. They compare these ratios with supernova yield models and find that a significant contribution from stars with masses >20 M$_\odot$ are needed to reach [α/Fe] ratios $\gtrsim$0.4 dex. In a comparable scenario to the one in NGC 5128, to explain the high [α/Fe] ratios in the elliptical galaxies, they proposed that in order to produce this amount of enriched material one needs to consider stellar populations composed of high-mass stars only, truncating the lower end of the IMF (<20 M$_\odot$), in combination with a relatively high SFR (Goodwin & Pagel 2005; Puzia et al. 2006). We point out that these empirical results appear only in their early-type galaxy sample, and is absent in the spirals studied as part of their work, suggesting an intrinsic difference in the formation histories of different galaxy types.

As shown with yellow points in Fig. 9, recent studies have found higher metallicities, [Fe/H], and enhanced [α/Fe] ratios for stars in the MW bulge (Matteucci & Brocato 1990; Bensby et al. 2013; Johnson et al. 2014; Gonzalez et al. 2015), similar to what is observed for the [Mg/Fe] and [Ti/Fe] ratios in the metal-rich GCs in NGC 5128. In principle, this might suggest similar formation histories with rapid chemical enrichment for NGC 5128 and the MW bulge. Photometric observations of halo stars in NGC 5128 analysed by Rejkuba et al. (2011) appear to support a rapid chemical enrichment scenario. Rejkuba et al. (2011) find that their CMD observations agree with older populations with high metallicities and enhanced α abundances.

We point out that previous abundance studies of GCs in NGC 5128 using line indices and low-resolution spectroscopic observations have not always found higher [α/Fe] ratios than in the MW. Beasley et al. (2008) and Woodley et al. (2010) estimated that the mean [α/Fe] ratios of the GC system in NGC 5128 are lower than the mean ratios measured in the MW. However, this conclusion is not unexpected given the large systematic uncertainties accompanying line index studies (Brodie & Strader 2006).

By visually inspecting Fig. 9, it appears that the [Mg/Fe] ratios throughout the whole metallicity range are more enhanced than [Ca/Fe] and [Ti/Fe]. As pointed out above, this behaviour has been observed in previous studies of dSph galaxies. Assuming this slight enhancement seen in [Mg/Fe] is not artificial, one possible explanation for differences between [(Ca, Ti)/Fe] and [Mg/Fe] is the lack of hypernovae in NGC 5128. According to Nakamura et al. (2001), the α-process takes place in hypernovae, creating ^{44}Ca and ^{48}Ti. Therefore, an environment with a lower number of hypernovae would appear to have lower [Ca/Fe] and [Ti/Fe] ratios, compared to [Mg/Fe]. This was the explanation suggested by Venn et al. (2004) for the difference in abundance ratios for [(Ca, Ti)/Fe] and [Mg/Fe] in dSphs.

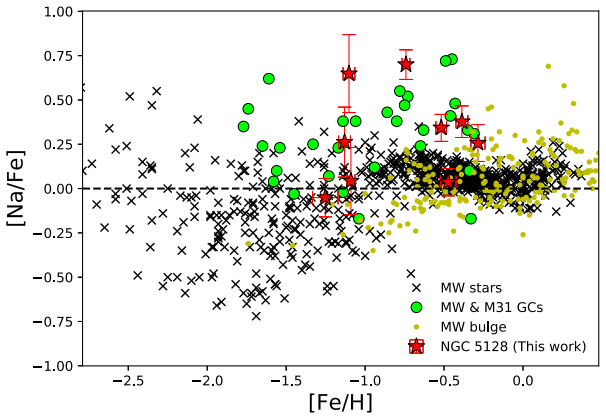

Figure 10. [Na/Fe] abundance ratios as a function of [Fe/H]. Symbols similar to Fig. 9, with the exception of green circles here are integrated-light measurements of GCs in the MW and M31 by Colucci et al. (2014, 2016).

5.2 Light elements: Na

We are able to measure [Na/Fe] abundance ratios for 9 out of the 20 clusters studied in this work. Light elements in general are of special interest given that recent studies have shown that these might not be entirely monometallic in GC populations, compared to [Fe/H] and other α-elements. We further discuss the observed star-to-star variations in GCs in Section 5.4.

We measured Na abundances using two wavelength bins, 5670–5700 and 6148–6168 Å covering the Na doublets 5682/5688 and 6154/6160 Å, respectively. This element is particularly difficult to measure as these lines are relatively weak. Given the quality of the spectra in the wavelength range of 5670–5700 Å, the strongest of the two doublets, we are only able to measure Na abundances for nine clusters. We note, however, that measurements for both bins are only available for seven out of these nine clusters. Whenever Na abundances are available for both bins, 5670–5700 and 6148–6168 Å, we find consistent Na measurements between the bins. In Fig. 10, we show our measured [Na/Fe] ratios as a function of metallicity. We see clearly elevated [Na/Fe] ratios in at least five GCs in NGC 5128, with higher values than those measured in field stars in the MW. Of course we currently do not have information about Na abundances of individual stars in NGC 5128; however, similar enhancements have been measured in integrated-light spectra of GCs in the MW and M 31, shown as green circles in Fig. 10 (Colucci et al. 2014, 2016).

Clear correlations have been observed in Na and O abundances in MW GCs and extragalactic ones. We look for possible correlations between Na and any of the α- and Fe-peak elements studied here, but find no such behaviour.

5.3 Fe-peak elements

In this section, we present our measurements for the Fe-peak elements: Cr, Mn, and Ni. In general, Fe-peak elements are suggested to be produced in SN Ia, however it is still not clear if all of the elements form in the same nucleosynthetic process. In spite of that, Fe-peak elements are of interest since they track the production of Fe (Iwamoto et al. 1999).

Studies of Galactic stars show that the [Cr/Fe] abundance ratios are very close to [Cr/Fe] ~ 0 throughout most of the metallicity coverage, as seen in the top panel of Fig. 11. For NGC 5128, we also see that the measured [Cr/Fe] are close to 0, within the errors of the individual measurements. However, we see an overall trend

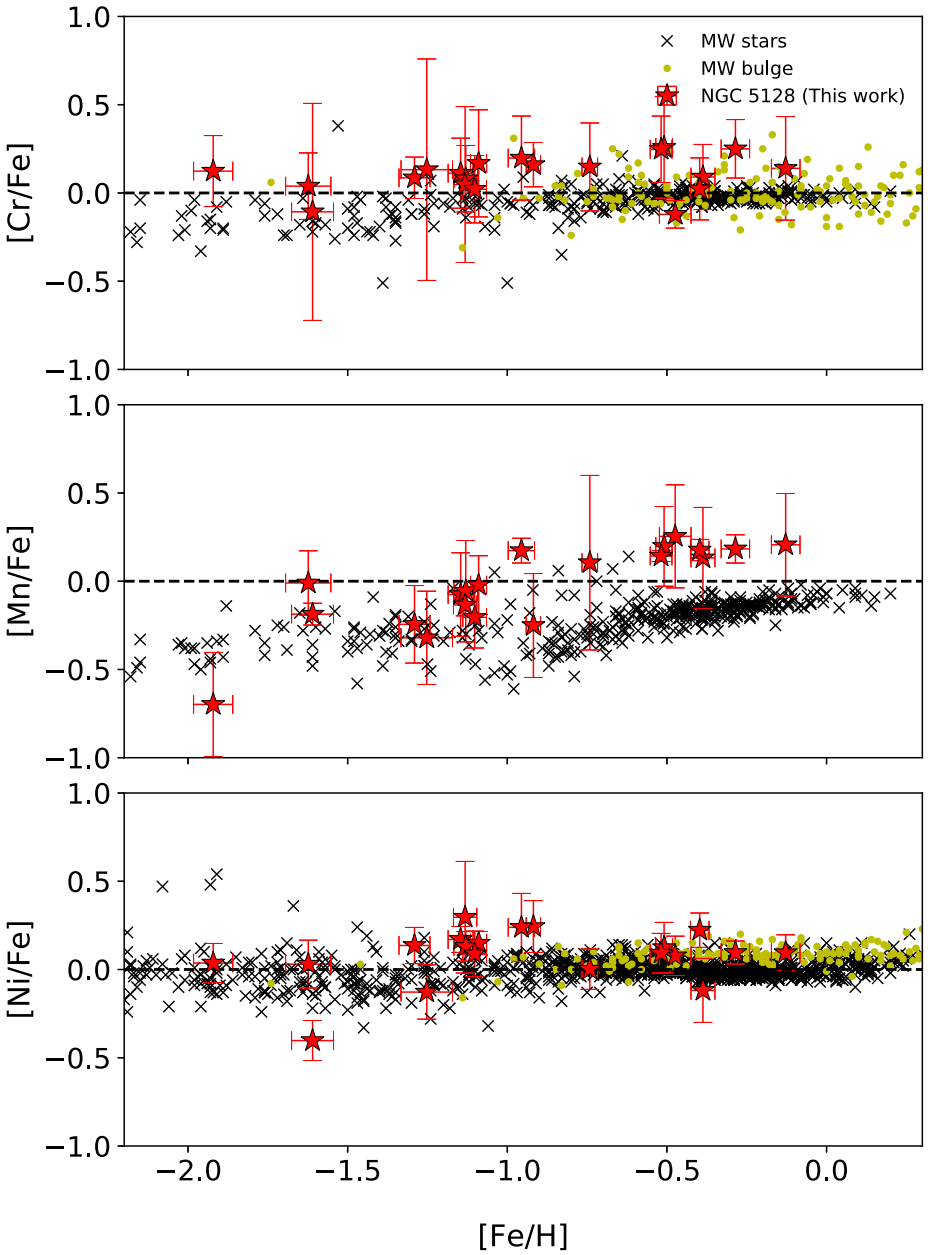

Figure 11. Top: [Cr/Fe] versus [Fe/H]. Middle: [Mn/Fe] versus [Fe/H]. Bottom: [Ni/Fe] versus [Fe/H]. Symbols as in Fig. 9.

where the [Cr/Fe] values for NGC 5128 are slightly above solar. We measure a weighted mean of [Cr/Fe] $= +0.06 \pm 0.02$ for the full GC sample in NGC 5128, slightly higher than the mean ratio observed in MW field stars, [Cr/Fe] $= -0.05 \pm 0.01$. The mean [Cr/Fe] seen in NGC 5128 is more comparable to that measured for the MW bulge stars, [Cr/Fe] $= +0.01 \pm 0.01$ (Fig. 11, yellow points), and certainly found within the spread of measured [Cr/Fe] in the Galactic bulge.

Although most of the Fe-peak elements behave somewhat similarly with Fe ratios close to 0, it is well known that Mn is depleted by ~ -0.5 dex in some metal-poor MW halo stars and GCs (Gratton et al. 1989; Sobeck et al. 2006; Romano, Cescutti & Matteucci 2011), including extragalactic GCs (see middle panel in Fig. 11). The MW [Mn/Fe] ratios appear to increase towards solar values at higher metallicities. This behaviour has not been well understood, especially since the actual formation of Mn continues to be uncertain (Timmes, Woosley & Weaver 1995; Shetrone et al. 2003). However, a possible explanation for this trend is that Mn is underproduced in SN II but overproduced in SN Ia, or a more accepted scenario is that the amount of Mn created is dependent on the metallicity of the progenitor (Gratton et al. 1989). Given that several studies find that this trend in [Mn/Fe] could be caused by NLTE effects (Battistini & Bensby 2015; Bergemann 2008), we then make relative comparisons of our measured [Mn/Fe] to studies assuming LTE. It appears that once the NLTE corrections are applied, the trend disappears and follows a similar behaviour as the other Fe-peak elements.

Regarding our abundance measurements for NGC 5128 from Fig. 11, we can visually identify a trend of low [Mn/Fe] ratios at low metallicities, increasing towards solar, and above solar, at higher [Fe/H]. Although this is in agreement with similar trends observed

in MW Galactic star and GC LTE studies, we see a slight offset in the trend of GCs in NGC 5128 compared to that of Galactic stars. For metallicities [Fe/H] > -1.0 dex, the [Mn/Fe] seem to reach higher abundances than the average MW field star population.

Ni also shows a relatively flat trend, with [Ni/Fe] abundance ratios close to 0, as shown in red stars in the bottom panel of Fig. 11. The overall trend seen in our [Ni/Fe] ratios for NGC 5128 is consistent with that of studies in the MW. Taking the weighted mean values of the full GC sample in NGC 5128, we measure [Ni/Fe] $= +0.09 \pm 0.04$, compared to a slightly lower mean [Ni/Fe] ratio of -0.02 ± 0.01 for MW field stars.

Overall, we find that our Fe-peak abundances follow similar trends as those seen in MW field stars, however, we identify a slight enhancement in the Fe-peak measurements from the GC system in NGC 5128.

5.4 Multiple populations in GCs

Studies have shown that the [Mg/Fe] abundance ratios of field stars in the MW, LMC, and M 31 behave similarly to other α-elements (Bensby et al. 2005; Colucci et al. 2009; Gonzalez et al. 2011). However, in the last decades in-depth research on individual stellar abundances in GCs has presented results that suggest the presence of intracluster Mg variations with respect to α-elements in several Galactic clusters (Shetrone 1996; Kraft et al. 1997; Gratton, Sneden & Carretta 2004). Furthermore, integrated-light studies of extragalactic GCs appear to also detect these same variations in Mg as lower [Mg/Fe] when compared to other [α/Fe] ratios. Through a study of the integrated light of 31 GCs in M 31, Colucci et al. (2014) find evidence for intracluster Mg variations. More specifically, they find that the more metal-poor, [Fe/H] < -0.7, GCs in M 31 are biased to low [Mg/Fe] ratios, hinting at a depletion of Mg. They measure [Mg/Fe] $\lesssim 0.0$ for GCs with metallicities [Fe/H] < -1.5. Similarly, studying the integrated light of extragalactic GCs in Fornax, Larsen et al. (2012) measure lower [Mg/Fe] than [Ca/Fe] and [Ti/Fe]. From Fig. 9, we clearly see that even in the low-metallicity regime, the [Mg/Fe] values are comparable to, or even higher than, those measured for [Ca/Fe] and [Ti/Fe]. Compared to the observations of Colucci et al. (2014) regarding the metal-poor GCs in M 31, we instead measure [Mg/Fe] ratios above solar abundances. These values suggest an absence of intracluster Mg variations in the GC populations in NGC 5128.

Similar to Mg, Na has exhibited star-to-star abundance variations in the GC population in the MW (for a recent review, see Gratton et al. 2004). In the last years, studies have found indirect evidence for abundance variations in extragalactic GCs (M 31, LMC, WLM, and IKN) that support the idea of intracluster abundance variations in Na (Colucci et al. 2009; Mucciarelli et al. 2009; Larsen et al. 2014). Specifically for Na, these intracluster variations are perceived as significantly elevated [Na/Fe] in integrated-light analysis of both galactic and extragalactic GCs. We find elevated [Na/Fe] abundance ratios for five GCs in NGC 5128, shown as red stars in Fig. 10. The enhancement in these GCs is higher than any abundances previously measured in any MW field stars, halo, disc or bulge. From the context of multiple populations in GCs, these enhancement in the Na abundances can in principle show evidence of star-to-star variations.

6 CONCLUSIONS

Through the analysis of integrated-light observations taken with the X-Shooter spectrograph on ESO's VLT and synthetic spectra created based on theoretical α-enhanced isochrones by the Dartmouth group, we obtain accurate metallicities for 20 GCs. The GCs studied here have metallicities ranging between [Fe/H] $= -1.92$ and -0.13 dex. We measure α-elements (Mg, Ca, and Ti), as well as a single light element (Na), and Fe-peak elements (Cr, Mn, and Ni). The new results of our work can be summarized as follows:

(i) Comparing our inferred metallicities to measurements from Beasley et al. (2008), we find excellent agreement between both works.

(ii) When comparing the four GC [Ca/Fe] abundance measurements to those by Colucci et al. (2013), we find that three out of four clusters are in good agreement, within 1σ. The [Ca/Fe] measurement of the fourth GC in Colucci et al. (2013) appears to be a 3σ outlier compared to our inferred abundances.

(iii) We find higher enhancement (~ 0.1 dex) in α-elements for the metal-poor ([Fe/H < -0.75 dex) GCs in NGC 5128, than what is observed in the MW. This could hint at a top-heavy IMF, a scenario supported by SAMs of galactic chemical evolution of early-type galaxies. Arrigoni et al. (2010) find that a slightly top-heavy IMF is essential to match the observations with models. However, we recommend to extend the GC sample size to firmly confirm such a scenario.

(iv) We find [Mg/Fe] ratios to be slightly higher than the [Ca/Fe] and [Ti/Fe] ratios. We suggest a lack of hypernovae in NGC 5128 as a possible explanation for this difference.

(v) In the context of multiple populations of GCs in NGC 5128, we measure Na in nine clusters. We find enhanced [Na/Fe] ratios for five GCs in our sample, providing evidence of star-to-star variations in these GCs. We find an absence of intracluster Mg variations in all 20 clusters.

(vi) We obtain the first measurements of Cr, Mn, and Ni for 20 GCs in NGC 5128, and find that the overall abundances follow similar trends as those seen in the MW field stars. We see a slight enhancement (<0.1 dex) in the mean Fe-peak abundances, when compared to those seen in the MW.

We point out that the work presented here is based on GC observations with exposure times of $\lesssim$30 min. Longer exposure times would provide better S/N on all three X-Shooter arms, increasing the integrated-light analysis potential especially for the NIR wavelengths. Such a coverage would allow for an in-depth study of the Al lines (i.e. 13123.38 and 13150.71 Å) providing information on possible [Al/Fe] enhancements similar to those observed in Galactic GCs, contributing to our discussion of multiple populations in extragalactic GCs.

The general agreement between existing metallicities and Ca abundance measurements and those presented as part of this work is extremely encouraging for future integrated-light analysis, reassuring that reliable metallicities and detailed chemical abundances can be obtained using intermediate-resolution observations.

ACKNOWLEDGEMENTS

We thank A. Gonneau, Y.-P. Chen, and M. Dries for their help and guidance during the X-Shooter reduction process. This research has made use of the NASA/IPAC Extragalactic Database, which is operated by the Jet Propulsion Laboratory, California Institute of Technology, under contract with the National Aeronautics and Space Administration. This is based on observations made with ESO telescopes at the La Silla Paranal Observatory under programme ID 085.B-0107(A).

REFERENCES

Arrigoni M., Trager S. C., Somerville R. S., Gibson B. K., 2010, MNRAS, 402, 173
Battistini C., Bensby T., 2015, A&A, 577, A9
Beasley M., Bridges T., Peng E., Harris W. E., Harris G. L. H., Forbes D. A., Mackie G., 2008, MNRAS, 386, 1443
Bensby T., Feltzing S., Lundström I., Ilyin I., 2005, A&A, 433, 185
Bensby T. et al., 2013, A&A, 549, A147
Bergemann M., 2008, Phys. Scr. Vol. T, 133, 014013
Bergemann M., Kudritzki R.-P., Gazak Z., Davies B., Plez B., 2015, ApJ, 804, 113
Bresolin F., 2008, The Metal-Rich Universe. Cambridge Univ. Press, Cambridge, UK, p. 155
Bressan A., Marigo P., Girardi L., Salasnich B., Dal Cero C., Rubele S., Nanni A., 2012, MNRAS, 427, 127
Brodie J. P., Strader J., 2006, ARA&A, 44, 193
Burstein D., Faber S. M., Gaskell C. M., Krumm N., 1984, ApJ, 287, 586
Cameron S. A., 2009, PhD thesis, University of Michigan
Castelli F., Gratton R. G., Kurucz R. L., 1997, A&A, 318, 841
Chen Y., Trager S. C., Peletier R. F., Lançon A., Vazdekis A., Prugniel Ph., Silva D. R., Gonneau A., 2014, A&A, 565, A117
Choi J., Dotter A., Conroy C., Cantiello M., Paxton B., Johnson B. D., 2016, ApJ, 823, 102
Colucci J. E., Bernstein R. A., Cameron S., McWilliam A., Cohen J. G., 2009, ApJ, 704, 385
Colucci J. E., Bernstein R. A., Cameron S. A., McWilliam A., 2011, ApJ, 735, 55
Colucci J. E., Duran M. F., Bernstein R. A., McWilliam A., 2013, ApJ, 773, 36
Colucci J. E., Bernstein R. A., Cohen J. G., 2014, ApJ, 797, 116
Colucci J. E., Bernstein R. A., McWilliam A., 2016, ApJ, 834, 105
Dotter A., 2016, ApJS, 222, 8
Dotter A., Chaboyer B., Jevremović D., Baron E., Ferguson J. W., Sarajedini A., Anderson J., 2007, AJ, 134, 376
Fisher D., Franx M., Illingworth G., 1995, ApJ, 448, 119
Gonzalez O. A. et al., 2011, A&A, 530, A54
Gonzalez O. A. et al., 2015, A&A, 584, A46
Goodwin S. P., Pagel B. E. J., 2005, MNRAS, 359, 707
Gratton R. G., 1989, A&A, 208, 171
Gratton R., Sneden C., Carretta E., 2004, ARA&A, 42, 385
Grevesse N., Sauval A. J., 1998, Space Sci. Rev., 85, 161
Gustafsson B., Edvardsson B., Eriksson K., Jørgensen U. G., Nordlund Å., Plez B., 2008, A&A, 486, 951
Harris W. E., 1991, ARA&A, 29, 543
Harris W. E., 1996, AJ, 112, 1487
Harris G. L. H., Rejkuba M., Harris W. E., 2010, PASA, 27, 457
Hernandez S., Larsen S., Trager S., Groot P., Kaper L., 2017, A&A, 603, A119
Hernandez S., Larsen S., Trager S., Kaper L., Groot P., 2018, MNRAS, 473, 826
Horne K., 1986, PASP, 98, 609
Ishigaki M. N., Aoki W., Chiba M., 2013, ApJ, 771, 67
Iwamoto K., Brachwitz F., Nomoto K., Kishimoto N., Umeda H., Hix W. R., Thielemann F.-K., 1999, ApJS, 125, 439
Johnson C. I., Rich R. M., Kobayashi C., Kunder A., Koch A., 2014, AJ, 148, 67
Kennicutt R. C., Jr, et al., 2003, PASP, 115, 928
Kewley L. J., Ellison S. L., 2008, ApJ, 681, 1183
Kraft R. P., Sneden C., Smith G. H., Shetrone M. D., Langer G.E, Pilachowski C. A., 1997, AJ, 113, 279-95
Kuntschner H., 2000, MNRAS, 315, 184
Kurucz R. L., 1970, SAO Spec. Rep. #309
Kurucz R. L., Avrett E. H., 1981, SAO Spec. Rep. #391
Kurucz R. L., Furenlid I., 1979, SAO Spec. Rep. #387
Larsen S., Brodie J. P., Strader J., 2012, A&A, 546, A53 (L12)
Larsen S., Brodie J. P, Forbes D. A., Strader J., 2014, A&A, 565, A98
Larsen S., Brodie J. P., Strader J., 2017, A&A, 601, 96
Lee J. C., Salzer J. J., Melbourne J., 2004, ApJ, 616, 752
López-Sánchez Á. R., Dopita M. A., Kewley L. J., Zahid H. J., Nicholls D. C., Scharwächter J., 2012, MNRAS, 426, 2630
Matteucci F., 2003, Astrophys. Space Sci., 284, 539
Matteucci F., Brocato E., 1990, ApJ, 365, 539
McWilliam A., 1997, ARA&A, 35, 503
McWilliam A., Bernstein R. A., 2008, ApJ, 684, 326
Mucciarelli A., Origlia L., Ferraro F. R., Pancino E., 2009, ApJ, 695, L134
Nakamura T., Umeda H., Iwamoto K., Nomoto K., Hashimoto M., Hix W. R., Thielemann F.-K., 2001, ApJ, 555, 880
Nomoto K., Iwamoto K., Kishimoto N., 1997, Science, 276, 1378
Olsen K A G, Miller B W, Suntzeff N B, Schommer R A, Bright J., 2004. AJ 127, 2674
Pierce M., Brodie J. P., Forbes D. A., Beasley M. A., Proctor R, Strader J., 2005, MNRAS, 358, 419
Pilachowski C. A., Sneden C., Kraft R. P., 1996, AJ, 111, 1689
Plez B., 2012, Astrophysics Source Code Library, record ascl:1205.004
Pritzl B. J., Venn K. A., Irwin M., 2005, AJ, 130, 2140
Proctor R. N., Sansom A. E., 2002, MNRAS, 333, 517
Puzia T. H., Saglia R. P., Kissler-Patig M., Maraston C., Greggio L., Renzini A., Ortolani S., 2002, A&A, 395, 45
Puzia T. H., Kissler-Patig M., Thomas D., Maraston C., Saglia R. P., Bender R., Goudfrooij P., Hempel P., 2005, A&A, 439, 997
Puzia T. H., Kissler-Patig M., Goudfrooij P., 2006, ApJ, 648, 383
Ramírez I., Allende Prieto C., 2011, ApJ, 743, 135
Reddy B. E., Tomkin J., Lambert D. L., Allende Prieto C., 2003, MNRAS, 340, 304
Reddy B. E., Lambert D. L., Allende Prieto C., 2006, MNRAS, 367, 1329
Rejkuba M., Dubath P., Minniti D., Meylan G., 2007, A&A, 469, 147
Rejkuba M., Harris W. E., Greggio L., Harris G. L. H., 2011, A&A, 526, A123
Romano D., Cescutti G., Matteucci F., 2011, MNRAS, 418, 696
Sakari C. M., Venn K. A., Mackey D., Shetrone M. D., Dotter A., Ferguson A. M. N., Huxor A., 2015, MNRAS, 448, 1314
Salpeter E. E., 1955, ApJ, 121, 161
Sarajedini A. et al., 2007, AJ, 133, 1658
Schiavon R. P., Rose J. A., Courteau S., MacArthur L. A., 2005, ApJS, 160, 163
Searle L., 1971, ApJ, 168, 327
Shetrone M. D., 1996, AJ, 112, 2639
Shetrone M. D., 2004, in McWilliam A., Rauch M. Eds., Origin and Evolution of the Elements from the Carnegie Observatories Centennial Symposia, Cambridge Univ. Press, Cambridge, UK, p. 220
Shetrone M. D., Bolte M., Stetson P. B., 1998, AJ, 115, 1888
Shetrone M., Venn K. A., Tolstoy E., Primas F., Hill V., Kaufer A., 2003, AJ, 125, 684
Sobeck J. S., Ivans I. I., Simmerer J. A., Sneden C., Hoeflich P., Hoeflich J. P., Kraft R. P., 2006, AJ, 131, 2949
Stasińska G., 2005, A&A, 434, 507
Strader J., Brodie J. P., Cenarro A. J., Beasley M. A., Forbes D. A., 2005, AJ, 130, 1315
Takeda Y., Sato B., Kambe E., Sadakane K., Ohkubo M., 2002, PASJ, 54, 1041
Taylor M. A., Puzia T. H., Harris G. L. H., Harris W. E., Kissler-Patig M., Hilker M., 2010, ApJ, 712, 119
Thomas D., Maraston C., Bender R., 2002, Ap&SS, 281, 371
Thomas D., Maraston C., Bender R., de Oliveira C. M., 2005, ApJ, 621, 673
Timmes F. X., Woosley S. E., Weaver T. A., 1995, ApJS, 98, 617
Tolstoy E., 2003, in Livio M., Noll K., Stiavelli M., eds, A Decade of Hubble Space Telescope Science. Cambridge Univ. Press, Cambridge, UK, p. 128
Trager S. C., Worthey G., Faber S. M., Burstein D., González J. J., 1998, ApJS, 116, 1
Trager S. C., Faber S. M., Worthey G., González J. J., 2000, AJ, 120, 165

van den Bosch R., de Zeeuw T., Gebhardt K., Noyola E., van de Ven G., 2006, ApJ, 641, 852
Venn K. A., 1999, ApJ, 518, 405
Venn K. A., Irwin M., Shetrone M. D., Tout C. A., Hill V., Tolstoy E., 2004, AJ, 128, 1177
Vernet et al., 2011, A&A, 536, A105
Wolf B., 1973, A&A, 28, 335
Woodley K. A., Harris W. E., Puzia T. H., Gómez M., Harris G. L. H., Geisler D., 2010, ApJ, 708, 1335
Woosley S. E., Weaver T. A., 1995, ApJS, 101, 181
Worthey G., 1998, PASP, 110, 888
Worthey G., Faber S. M., González J. J., 1992, ApJ, 398, 69
Worthey G., Faber S. M., Gonzá lez J. J., Burstein D., 1994, ApJS, 94, 687

APPENDIX A: METALLICITIES AS A FUNCTION OF WAVELENGTH

We present tables displaying the individual bin measurements for each of the YMCs studied in this work. Additionally, to visually appreciate the dispersion between the individual measurements for a corresponding element with multiple bins, in Figs A1–A5, we plot bin abundances as a function of wavelength for a selected sample of GCs.

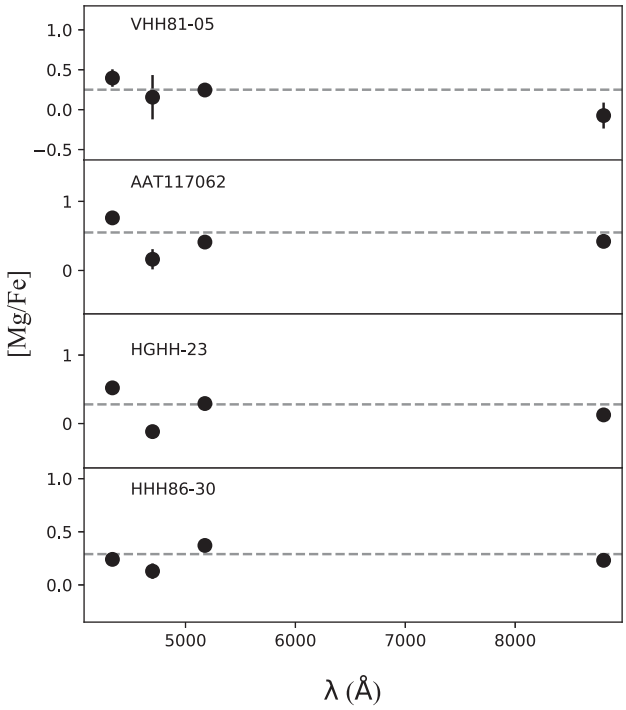

Figure A1. [Mg/Fe] abundances as a function of wavelength for a selected sample of GCs in NGC 5128.

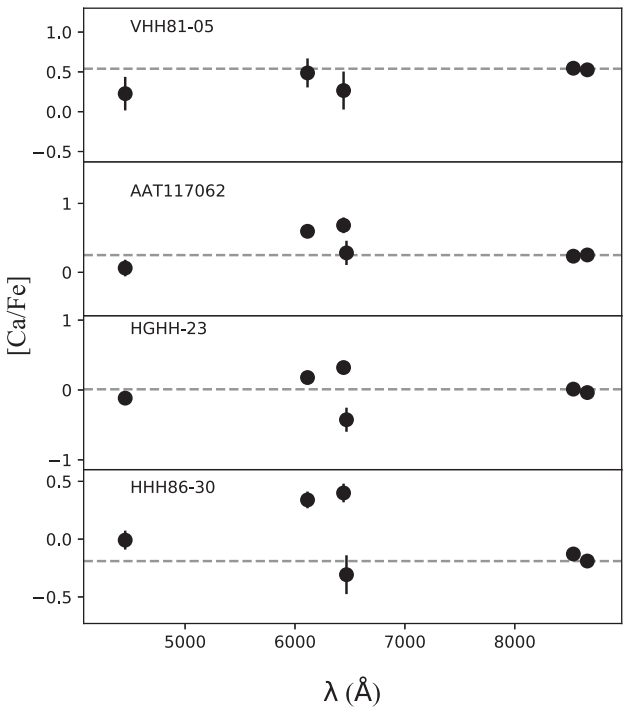

Figure A2. [Ca/Fe] abundances as a function of wavelength for a selected sample of GCs in NGC 5128.

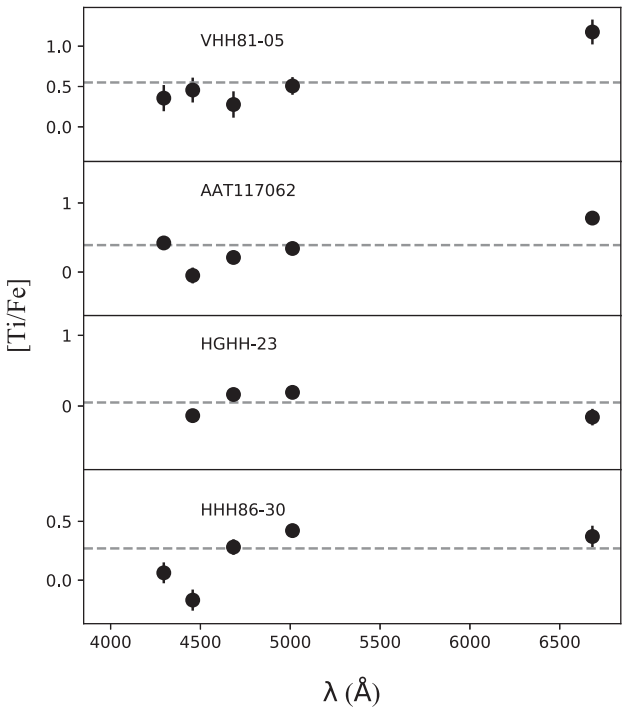

Figure A3. [Ti/Fe] abundances as a function of wavelength for a selected sample of GCs in NGC 5128.

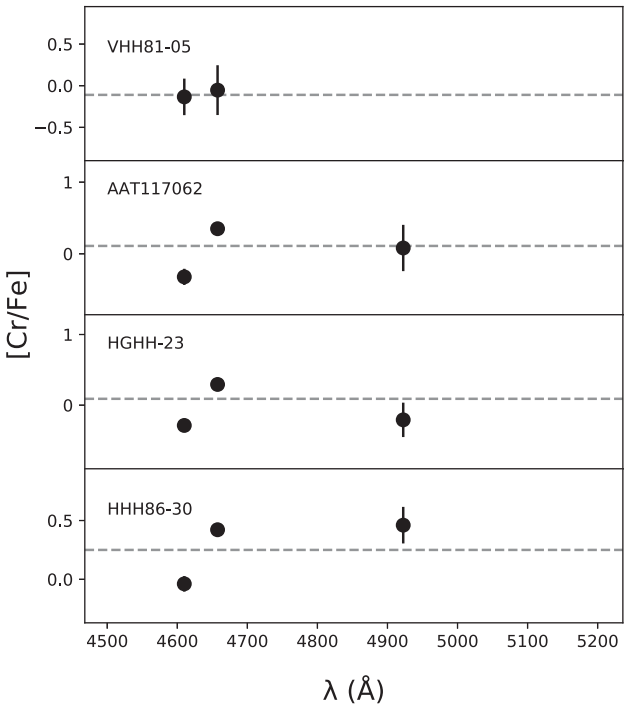

Figure A4. [Cr/Fe] abundances as a function of wavelength for a selected sample of GCs in NGC 5128.

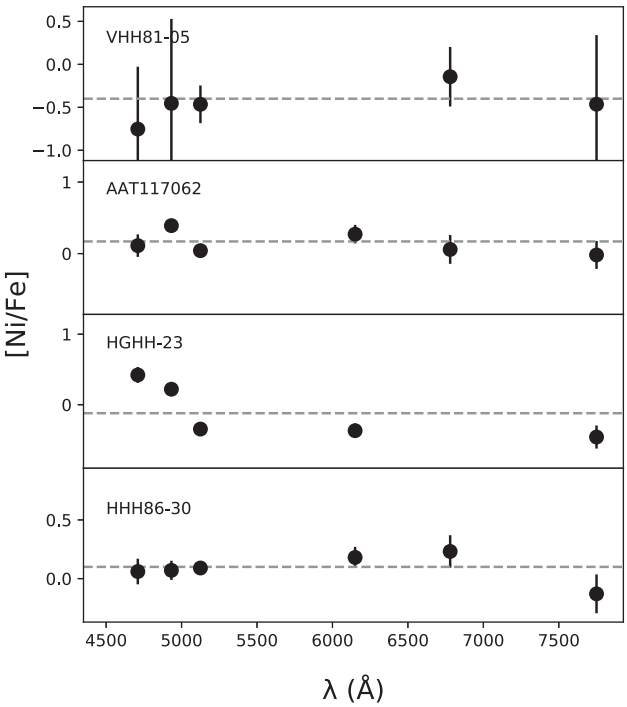

Figure A5. [Ni/Fe] abundances as a function of wavelength for a selected sample of GCs in NGC 5128.

Table A1. Chemical abundances AAT117062.

Element	Wavelength (Å)	Abundance	Error
[Fe/H]	4400.0–4600.0	−1.265	0.021
	4600.0–4800.0	−1.194	0.033
	4800.0–5000.0	−1.124	0.021
	5000.0–5200.0	−1.184	0.031
	6100.0–6300.0	−1.166	0.041
	6300.0–6500.0	−1.154	0.042
	6500.0–6700.0	−1.225	0.048
	6700.0–6800.0	−0.974	0.112
	7400.0–7550.0	−1.166	0.061
	8500.0–8700.0	−0.834	0.031
	8700.0–8850.0	−0.984	0.091
[Mg/Fe]	4300.0–4370.0	+0.761	0.054
	4690.0–4710.0	+0.162	0.146
	5150.0–5200.0	+0.411	0.058
	8777.0–8832.0	+0.421	0.066
[Ca/Fe]	4445.0–4465.0	+0.062	0.120
	6100.0–6128.0	+0.595	0.083
	6430.0–6454.0	+0.682	0.113
	6459.0–6478.0	+0.282	0.175
	8480.0–8586.0	+0.234	0.037
	8623.0–8697.0	+0.252	0.038
[Ti/Fe]	4270.0–4322.0	+0.421	0.088
	4440.0–4474.0	−0.050	0.115
	4650.0–4718.0	+0.211	0.090
	4980.0–5045.0	+0.341	0.062
	6584.0–6780.0	+0.781	0.080
[Na/Fe]	5670.0–5700.0	–	–
	6148.0–6168.0	–	–
[Cr/Fe]	4580.0–4640.0	−0.322	0.112
	4640.0–4675.0	+0.350	0.087
	4915.0–4930.0	+0.081	0.323
[Mn/Fe]	4450.0–4515.0	−0.438	0.205
	4750.0–4770.0	−0.030	0.115
[Ni/Fe]	4700.0–4720.0	+0.111	0.157
	4910.0–4955.0	+0.391	0.091
	5075.0–5175.0	+0.041	0.078
	6100.0–6200.0	+0.271	0.130
	6760.0–6800.0	+0.058	0.201
	7700.0–7800.0	−0.018	0.195

Table A2. Chemical abundances HGHH-04.

Element	Wavelength (Å)	Abundance	Error
[Fe/H]	4400.0–4600.0	−2.004	0.082
	4600.0–4800.0	−1.824	0.092
	4800.0–5000.0	−1.904	0.062
	5000.0–5200.0	−1.945	0.061
	6100.0–6300.0	−1.535	0.091
	6300.0–6500.0	−2.014	0.112
	6500.0–6700.0	−1.963	0.192
	6700.0–6800.0	−1.834	0.322
	7400.0–7550.0	−2.184	0.212
	8500.0–8700.0	−2.323	0.112
	8700.0–8850.0	−1.865	0.181
[Mg/Fe]	4300.0–4370.0	–	–
	4690.0–4710.0	+0.116	0.355
	5150.0–5200.0	+0.467	0.083
	8777.0–8832.0	−0.093	0.337
[Ca/Fe]	4445.0–4465.0	−0.083	0.385
	6100.0–6128.0	+0.778	0.219
	6430.0–6454.0	+0.778	0.229
	6459.0–6478.0	+0.046	0.572
	8480.0–8586.0	+0.527	0.057
	8623.0–8697.0	+0.507	0.064
[Ti/Fe]	4270.0–4322.0	+0.608	0.191
	4440.0–4474.0	+0.707	0.21
	4650.0–4718.0	+0.367	0.238
	4980.0–5045.0	+0.437	0.143
	6584.0–6780.0	+0.267	1.791
[Na/Fe]	5670.0–5700.0	–	–
	6148.0–6168.0	–	–
[Cr/Fe]	4580.0–4640.0	+0.098	0.278
	4640.0–4675.0	+0.118	0.376
	4915.0–4930.0	+0.687	1.212
[Mn/Fe]	4450.0–4515.0	−0.153	2.173
	4750.0–4770.0	−0.732	0.545
[Ni/Fe]	4700.0–4720.0	+0.297	0.356
	4910.0–4955.0	+0.067	0.844
	5075.0–5175.0	−0.192	0.278
	6100.0–6200.0	−0.004	0.355
	6760.0–6800.0	−0.223	0.605
	7700.0–7800.0	+0.328	0.386

Table A3. Chemical abundances HGHH-06.

Element	Wavelength (Å)	Abundance	Error
[Fe/H]	4400.0–4600.0	−0.955	0.041
	4600.0–4800.0	−0.855	0.063
	4800.0–5000.0	−0.876	0.038
	5000.0–5200.0	−0.995	0.061
	6100.0–6300.0	−0.886	0.076
	6300.0–6500.0	−0.925	0.090
	6500.0–6700.0	−0.955	0.109
	6700.0–6800.0	−1.055	0.241
	7400.0–7550.0	−0.835	0.090
	8500.0–8700.0	−0.996	0.067
	8700.0–8850.0	−0.824	0.136
[Mg/Fe]	4300.0–4370.0	+0.792	0.092
	4690.0–4710.0	+0.523	0.166
	5150.0–5200.0	+0.632	0.054
	8777.0–8832.0	+0.584	0.084
[Ca/Fe]	4445.0–4465.0	−0.077	0.211
	6100.0–6128.0	+0.857	0.096
	6430.0–6454.0	+0.793	0.134
	6459.0–6478.0	+0.054	0.293
	8480.0–8586.0	+0.346	0.025
	8623.0–8697.0	+0.304	0.024
[Ti/Fe]	4270.0–4322.0	+0.063	0.178
	4440.0–4474.0	+0.084	0.172
	4650.0–4718.0	+0.483	0.122
	4980.0–5045.0	+0.293	0.074
	6584.0–6780.0	+0.503	0.114
[Na/Fe]	5670.0–5700.0	–	–
	6148.0–6168.0	–	–
[Cr/Fe]	4580.0–4640.0	+0.012	0.141
	4640.0–4675.0	+0.292	0.144
	4915.0–4930.0	+0.433	0.492
[Mn/Fe]	4450.0–4515.0	−0.736	0.451
	4750.0–4770.0	−0.149	0.208
[Ni/Fe]	4700.0–4720.0	−0.003	0.269
	4910.0–4955.0	+0.593	0.147
	5075.0–5175.0	+0.243	0.103
	6100.0–6200.0	+0.123	0.192
	6760.0–6800.0	−0.487	0.281
	7700.0–7800.0	+0.214	0.282

Table A4. Chemical abundances HGHH-07.

Element	Wavelength (Å)	Abundance	Error
[Fe/H]	4400.0–4600.0	−1.284	0.025
	4600.0–4800.0	−1.112	0.033
	4800.0–5000.0	−1.086	0.023
	5000.0–5200.0	−1.134	0.026
	6100.0–6300.0	−1.013	0.043
	6300.0–6500.0	−0.929	0.050
	6500.0–6700.0	−1.055	0.078
	6700.0–6800.0	−1.244	0.172
	7400.0–7550.0	−1.125	0.076
	8500.0–8700.0	−1.196	0.046
	8700.0–8850.0	−0.886	0.090
[Mg/Fe]	4300.0–4370.0	+0.924	0.064
	4690.0–4710.0	+0.456	0.116
	5150.0–5200.0	+0.486	0.041
	8777.0–8832.0	+0.376	0.070
[Ca/Fe]	4445.0–4465.0	+0.116	0.116
	6100.0–6128.0	+0.807	0.077
	6430.0–6454.0	+0.596	0.125
	6459.0–6478.0	−0.005	0.219
	8480.0–8586.0	+0.505	0.036
	8623.0–8697.0	+0.436	0.036
[Ti/Fe]	4270.0–4322.0	+0.104	0.133
	4440.0–4474.0	+0.056	0.120
	4650.0–4718.0	+0.484	0.087
	4980.0–5045.0	+0.215	0.070
	6584.0–6780.0	+0.414	0.109
[Na/Fe]	5670.0–5700.0	+0.145	0.193
	6148.0–6168.0	+0.534	0.292
[Cr/Fe]	4580.0–4640.0	−0.054	0.097
	4640.0–4675.0	+0.224	0.129
	4915.0–4930.0	+0.585	0.276
[Mn/Fe]	4450.0–4515.0	−0.505	0.252
	4750.0–4770.0	+0.065	0.134
[Ni/Fe]	4700.0–4720.0	+0.044	0.194
	4910.0–4955.0	+0.224	0.134
	5075.0–5175.0	−0.005	0.095
	6100.0–6200.0	+0.245	0.146
	6760.0–6800.0	+0.495	0.193
	7700.0–7800.0	+0.047	0.222

Table A5. Chemical abundances HGHH-11.

Element	Wavelength (Å)	Abundance	Error
[Fe/H]	4400.0–4600.0	−0.444	0.012
	4600.0–4800.0	−0.126	0.028
	4800.0–5000.0	−0.585	0.021
	5000.0–5200.0	−0.624	0.031
	6100.0–6300.0	−0.574	0.042
	6300.0–6500.0	−0.546	0.047
	6500.0–6700.0	−0.755	0.079
	6700.0–6800.0	−0.654	0.092
	7400.0–7550.0	−0.656	0.058
	8500.0–8700.0	−0.484	0.042
	8700.0–8850.0	−0.624	0.07
[Mg/Fe]	4300.0–4370.0	+0.400	0.112
	4690.0–4710.0	+0.081	0.128
	5150.0–5200.0	+0.468	0.061
	8777.0–8832.0	+0.090	0.069
[Ca/Fe]	4445.0–4465.0	+0.004	0.126
	6100.0–6128.0	+0.103	0.089
	6430.0–6454.0	−0.020	0.112
	6459.0–6478.0	−0.649	0.224
	8480.0–8586.0	−0.076	0.046
	8623.0–8697.0	−0.120	0.047
[Ti/Fe]	4270.0–4322.0	−0.160	0.158
	4440.0–4474.0	+0.000	0.130
	4650.0–4718.0	+0.260	0.098
	4980.0–5045.0	+0.230	0.084
	6584.0–6780.0	−0.511	0.215
[Na/Fe]	5670.0–5700.0	+0.064	0.184
	6148.0–6168.0	−0.059	0.326
[Cr/Fe]	4580.0–4640.0	−0.241	0.102
	4640.0–4675.0	−0.022	0.094
	4915.0–4930.0	−0.151	0.323
[Mn/Fe]	4450.0–4515.0	−0.158	0.180
	4750.0–4770.0	+0.419	0.119
[Ni/Fe]	4700.0–4720.0	+0.159	0.166
	4910.0–4955.0	+0.319	0.119
	5075.0–5175.0	−0.252	0.118
	6100.0–6200.0	+0.222	0.122
	6760.0–6800.0	−0.260	0.206
	7700.0–7800.0	+0.145	0.200

Table A6. Chemical abundances HGHH-17.

Element	Wavelength (Å)	Abundance	Error
[Fe/H]	4400.0–4600.0	−1.194	0.022
	4600.0–4800.0	−1.080	0.035
	4800.0–5000.0	−1.055	0.030
	5000.0–5200.0	−1.025	0.030
	6100.0–6300.0	−0.946	0.044
	6300.0–6500.0	−1.124	0.052
	6500.0–6700.0	−1.114	0.071
	6700.0–6800.0	−0.974	0.102
	7400.0–7550.0	−0.997	0.069
	8500.0–8700.0	−1.126	0.037
	8700.0–8850.0	−0.934	0.066
[Mg/Fe]	4300.0–4370.0	+0.755	0.062
	4690.0–4710.0	+0.276	0.134
	5150.0–5200.0	+0.485	0.031
	8777.0–8832.0	+0.596	0.066
[Ca/Fe]	4445.0–4465.0	+0.316	0.094
	6100.0–6128.0	+0.492	0.085
	6430.0–6454.0	+0.745	0.104
	6459.0–6478.0	+0.167	0.172
	8480.0–8586.0	+0.455	0.026
	8623.0–8697.0	+0.427	0.027
[Ti/Fe]	4270.0–4322.0	+0.215	0.104
	4440.0–4474.0	+0.126	0.120
	4650.0–4718.0	+0.426	0.084
	4980.0–5045.0	+0.266	0.056
	6584.0–6780.0	+0.226	0.124
[Na/Fe]	5670.0–5700.0	+0.043	0.189
	6148.0–6168.0	–	–
[Cr/Fe]	4580.0–4640.0	−0.084	0.105
	4640.0–4675.0	+0.215	0.098
	4915.0–4930.0	+0.935	0.202
[Mn/Fe]	4450.0–4515.0	−0.235	0.175
	4750.0–4770.0	+0.095	0.130
[Ni/Fe]	4700.0–4720.0	+0.174	0.143
	4910.0–4955.0	+0.155	0.122
	5075.0–5175.0	−0.004	0.075
	6100.0–6200.0	+0.384	0.112
	6760.0–6800.0	+0.387	0.164
	7700.0–7800.0	+0.168	0.196

Table A7. Chemical abundances HGHH-21.

Element	Wavelength (Å)	Abundance	Error
[Fe/H]	4400.0–4600.0	−1.045	0.031
	4600.0–4800.0	−0.965	0.051
	4800.0–5000.0	−0.896	0.029
	5000.0–5200.0	−0.955	0.041
	6100.0–6300.0	−0.985	0.060
	6300.0–6500.0	−0.934	0.062
	6500.0–6700.0	−0.939	0.093
	6700.0–6800.0	−1.255	0.161
	7400.0–7550.0	−0.926	0.074
	8500.0–8700.0	−0.945	0.058
	8700.0–8850.0	−0.665	0.101
[Mg/Fe]	4300.0–4370.0	+0.531	0.102
	4690.0–4710.0	+0.253	0.177
	5150.0–5200.0	+0.616	0.059
	8777.0–8832.0	+0.431	0.073
[Ca/Fe]	4445.0–4465.0	+0.282	0.128
	6100.0–6128.0	+0.562	0.103
	6430.0–6454.0	+0.653	0.138
	6459.0–6478.0	+0.101	0.233
	8480.0–8586.0	+0.292	0.039
	8623.0–8697.0	+0.333	0.040
[Ti/Fe]	4270.0–4322.0	+0.210	0.168
	4440.0–4474.0	+0.152	0.137
	4650.0–4718.0	+0.532	0.100
	4980.0–5045.0	+0.282	0.079
	6584.0–6780.0	+0.708	0.088
[Na/Fe]	5670.0–5700.0	–	–
	6148.0–6168.0	–	–
[Cr/Fe]	4580.0–4640.0	+0.142	0.117
	4640.0–4675.0	+0.151	0.127
	4915.0–4930.0	+0.852	0.293
[Mn/Fe]	4450.0–4515.0	+0.241	0.191
	4750.0–4770.0	+0.123	0.166
[Ni/Fe]	4700.0–4720.0	−0.646	0.405
	4910.0–4955.0	+0.472	0.128
	5075.0–5175.0	−0.138	0.117
	6100.0–6200.0	+0.492	0.137
	6760.0–6800.0	+0.504	0.217
	7700.0–7800.0	+0.246	0.257

Table A8. Chemical abundances HGHH-23.

Element	Wavelength (Å)	Abundance	Error
[Fe/H]	4400.0–4600.0	−0.435	0.011
	4600.0–4800.0	−0.445	0.030
	4800.0–5000.0	−0.535	0.010
	5000.0–5200.0	−0.445	0.021
	6100.0–6300.0	−0.392	0.024
	6300.0–6500.0	−0.415	0.039
	6500.0–6700.0	−0.265	0.040
	6700.0–6800.0	−0.384	0.052
	7400.0–7550.0	−0.587	0.046
	8500.0–8700.0	−0.135	0.011
	8700.0–8850.0	−0.313	0.052
[Mg/Fe]	4300.0–4370.0	+0.521	0.051
	4690.0–4710.0	−0.118	0.097
	5150.0–5200.0	+0.292	0.042
	8777.0–8832.0	+0.126	0.047
[Ca/Fe]	4445.0–4465.0	−0.117	0.070
	6100.0–6128.0	+0.178	0.066
	6430.0–6454.0	+0.321	0.077
	6459.0–6478.0	−0.426	0.172
	8480.0–8586.0	+0.012	0.034
	8623.0–8697.0	−0.037	0.035
[Ti/Fe]	4270.0–4322.0	–	–
	4440.0–4474.0	−0.136	0.088
	4650.0–4718.0	+0.163	0.062
	4980.0–5045.0	+0.193	0.062
	6584.0–6780.0	−0.157	0.117
[Na/Fe]	5670.0–5700.0	+0.324	0.127
	6148.0–6168.0	+0.489	0.180
[Cr/Fe]	4580.0–4640.0	−0.287	0.074
	4640.0–4675.0	+0.293	0.058
	4915.0–4930.0	−0.208	0.243
[Mn/Fe]	4450.0–4515.0	−0.286	0.117
	4750.0–4770.0	+0.282	0.075
[Ni/Fe]	4700.0–4720.0	+0.422	0.112
	4910.0–4955.0	+0.220	0.088
	5075.0–5175.0	−0.345	0.071
	6100.0–6200.0	−0.368	0.103
	6760.06800.0	–	–
	7700.07800.0	−0.458	0.163

Table A9. Chemical abundances HGHH-29.

Element	Wavelength (Å)	Abundance	Error
[Fe/H]	4400.0–4600.0	−0.464	0.029
	4600.0–4800.0	−0.464	0.032
	4800.0–5000.0	−0.546	0.025
	5000.0–5200.0	−0.564	0.032
	6100.0–6300.0	−0.575	0.040
	6300.0–6500.0	−0.545	0.048
	6500.0–6700.0	−0.474	0.062
	6700.0–6800.0	−0.634	0.111
	7400.0–7550.0	−0.555	0.060
	8500.0–8700.0	−0.405	0.051
	8700.0–8850.0	−0.335	0.061
[Mg/Fe]	4300.0–4370.0	+0.393	0.119
	4690.0–4710.0	+0.194	0.133
	5150.0–5200.0	+0.463	0.046
	8777.0–8832.0	+0.425	0.055
[Ca/Fe]	4445.0–4465.0	−0.074 0	0.146
	6100.0–6128.0	+0.174	0.084
	6430.0–6454.0	+0.291	0.110
	6459.0–6478.0	+0.150	0.177
	8480.0–8586.0	+0.065	0.027
	8623.0–8697.0	−0.026	0.020
[Ti/Fe]	4270.0–4322.0	+0.004	0.151
	4440.0–4474.0	+0.174	0.129
	4650.0–4718.0	+0.405	0.104
	4980.0–5045.0	+0.313	0.084
	6584.0–6780.0	+0.323	0.140
[Na/Fe]	5670.0–5700.0	–	–
	6148.0–6168.0	–	–
[Cr/Fe]	4580.0–4640.0	+0.075	0.104
	4640.0–4675.0	+0.435	0.095
	4915.0–4930.0	−0.546	0.491
[Mn/Fe]	4450.0–4515.0	−0.105	0.202
	4750.0–4770.0	+0.344	0.141
[Ni/Fe]	4700.0–4720.0	+0.242	0.189
	4910.0–4955.0	+0.423	0.141
	5075.0–5175.0	−0.116	0.112
	6100.0–6200.0	−0.198	0.153
	6760.0–6800.0	−0.054	0.203
	7700.0–7800.0	+0.683	0.171

Table A10. Chemical abundances HGHH-34.

Element	Wavelength (Å)	Abundance	Error
[Fe/H]	4400.0–4600.0	−0.395	0.021
	4600.0–4800.0	−0.475	0.043
	4800.0–5000.0	−0.435	0.011
	5000.0–5200.0	−0.315	0.03
	6100.0–6300.0	−0.384	0.021
	6300.0–6500.0	−0.355	0.047
	6500.0–6700.0	−0.375	0.081
	6700.0–6800.0	−0.394	0.082
	7400.0–7550.0	−0.345	0.050
	8500.0–8700.0	−0.104	0.042
	8700.0–8850.0	−0.292	0.082
[Mg/Fe]	4300.0–4370.0	+0.381	0.083
	4690.0–4710.0	+0.102	0.122
	5150.0–5200.0	+0.482	0.057
	8777.0–8832.0	+0.177	0.069
[Ca/Fe]	4445.0–4465.0	+0.203	0.105
	6100.0–6128.0	+0.263	0.092
	6430.0–6454.0	+0.232	0.124
	6459.0–6478.0	+0.153	0.193
	8480.0–8586.0	+0.002	0.029
	8623.0–8697.0	−0.047	0.031
[Ti/Fe]	4270.0–4322.0	+0.293	0.114
	4440.0–4474.0	−0.158	0.123
	4650.0–4718.0	+0.242	0.102
	4980.0–5045.0	+0.942	0.067
	6584.0–6780.0	+0.183	0.096
[Na/Fe]	5670.0–5700.0	–	–
	6148.0–6168.0	–	–
[Cr/Fe]	4580.0–4640.0	−0.060	0.102
	4640.0–4675.0	+0.038	0.106
	4915.0–4930.0	+0.503	0.263
[Mn/Fe]	4450.0–4515.0	+0.112	0.183
	4750.0–4770.0	+0.221	0.152
[Ni/Fe]	4700.0–4720.0	+0.091	0.182
	4910.0–4955.0	+0.432	0.115
	5075.0–5175.0	+0.153	0.085
	6100.0–6200.0	−0.058	0.135
	6760.0–6800.0	+0.520	0.187
	7700.0–7800.0	+0.412	0.194

Table A11. Chemical abundances HGHH-40.

Element	Wavelength (Å)	Abundance	Error
[Fe/H]	4400.0–4600.0	−1.206	0.069
	4600.0–4800.0	−1.223	0.083
	4800.0–5000.0	−1.045	0.051
	5000.0–5200.0	−1.255	0.080
	6100.0–6300.0	−1.124	0.081
	6300.0–6500.0	−1.205	0.120
	6500.0–6700.0	−0.928	0.137
	6700.0–6800.0	−1.254	0.233
	7400.0–7550.0	−0.876	0.127
	8500.0–8700.0	−1.155	0.104
	8700.0–8850.0	−1.238	0.168
[Mg/Fe]	4300.0–4370.0	+0.118	0.332
	4690.0–4710.0	+0.108	0.362
	5150.0–5200.0	+0.337	0.097
	8777.0–8832.0	−0.073	0.174
[Ca/Fe]	4445.0–4465.0	−0.162	0.374
	6100.0–6128.0	+0.286	0.251
	6430.0–6454.0	+0.116	0.302
	6459.0–6478.0	+0.197	0.333
	8480.0–8586.0	+0.197	0.046
	8623.0–8697.0	+0.177	0.058
[Ti/Fe]	4270.0–4322.0	−0.002	0.254
	4440.0–4474.0	−0.313	0.293
	4650.0–4718.0	+0.118	0.222
	4980.0–5045.0	+0.478	0.124
	6584.0–6780.0	–	–
[Na/Fe]	5670.0–5700.0	–	–
	6148.0–6168.0	–	–
[Cr/Fe]	4580.0–4640.0	+0.207	0.193
	4640.0–4675.0	−0.593	0.382
	4915.0–4930.0	–	–
[Mn/Fe]	4450.0–4515.0	−0.072	0.393
	4750.0–4770.0	−0.173	0.308
[Ni/Fe]	4700.0–4720.0	–	–
	4910.0–4955.0	+0.688	0.190
	5075.0–5175.0	−1.023	0.472
	6100.0–6200.0	+0.068	0.254
	6760.0–6800.0	+0.206	0.350
	7700.0–7800.0	+0.246	0.242

Table A12. Chemical abundances HH-080.

Element	Wavelength (Å)	Abundance	Error
[Fe/H]	4400.0–4600.0	−1.825	0.058
	4600.0–4800.0	−1.716	0.075
	4800.0–5000.0	−1.696	0.036
	5000.0–5200.0	−1.696	0.045
	6100.0–6300.0	−1.536	0.088
	6300.0–6500.0	−1.286	0.077
	6500.0–6700.0	−1.454	0.122
	6700.0–6800.0	−1.326	0.442
	7400.0–7550.0	−1.192	0.096
	8500.0–8700.0	−1.714	0.102
	8700.0–8850.0	−1.465	0.161
[Mg/Fe]	4300.0–4370.0	+0.399	0.239
	4690.0–4710.0	−0.293	0.256
	5150.0–5200.0	−0.162	0.100
	8777.0–8832.0	+0.357	0.159
[Ca/Fe]	4445.0–4465.0	+0.057	0.198
	6100.0–6128.0	−0.110	0.211
	6430.0–6454.0	+0.0157	0.227
	6459.0–6478.0	+0.335	0.255
	8480.0–8586.0	+0.298	0.061
	8623.0–8697.0	+0.317	0.061
[Ti/Fe]	4270.0–4322.0	−0.083	0.170
	4440.0–4474.0	−0.223	0.199
	4650.0–4718.0	+0.077	0.180
	4980.0–5045.0	+0.199	0.094
	6584.0–6780.0	+0.588	0.322
[Na/Fe]	5670.0–5700.0	–	–
	6148.0–6168.0	–	–
[Cr/Fe]	4580.0–4640.0	−0.003	0.180
	4640.0–4675.0	−0.154	0.246
	4915.0–4930.0	−0.081	0.500
[Mn/Fe]	4450.0–4515.0	+0.188	0.263
	4750.0–4770.0	−0.184	0.198
[Ni/Fe]	4700.0–4720.0	−0.242	0.390
	4910.0–4955.0	+0.096	0.380
	5075.0–5175.0	−0.043	0.149
	6100.0–6200.0	+0.587	0.204
	6760.0–6800.0	+0.010	0.329
	7700.0–7800.0	+0.204	0.312

Table A13. Chemical abundances HH-096.

Element	Wavelength (Å)	Abundance	Error
[Fe/H]	4400.0–4600.0	−1.265	0.041
	4600.0–4800.0	−1.185	0.041
	4800.0–5000.0	−1.246	0.039
	5000.0–5200.0	−1.424	0.042
	6100.0–6300.0	−1.096	0.058
	6300.0–6500.0	−1.295	0.070
	6500.0–6700.0	−1.496	0.097
	6700.0–6800.0	−1.194	0.162
	7400.0–7550.0	−1.547	0.109
	8500.0–8700.0	−1.548	0.067
	8700.0–8850.0	−1.177	0.118
[Mg/Fe]	4300.0–4370.0	+0.704	0.108
	4690.0–4710.0	+0.317	0.217
	5150.0–5200.0	+0.337	0.068
	8777.0–8832.0	−0.323	0.157
[Ca/Fe]	4445.0–4465.0	+0.216	0.167
	6100.0–6128.0	+0.375	0.147
	6430.0–6454.0	+0.398	0.169
	6459.0–6478.0	+0.287	0.209
	8480.0–8586.0	+0.406	0.046
	8623.0–8697.0	+0.287	0.049
[Ti/Fe]	4270.0–4322.0	+0.236	0.147
	4440.0–4474.0	+0.407	0.139
	4650.0–4718.0	+0.347	0.120
	4980.0–5045.0	+0.166	0.092
	6584.0–6780.0	+0.454	0.229
[Na/Fe]	5670.0–5700.0	–	–
	6148.0–6168.0	–	–
[Cr/Fe]	4580.0–4640.0	+0.086	0.127
	4640.0–4675.0	+0.025	0.185
	4915.0–4930.0	+0.377	0.394
[Mn/Fe]	4450.0–4515.0	−0.624	0.502
	4750.0–4770.0	−0.194	0.186
[Ni/Fe]	4700.0–4720.0	−0.213	0.326
	4910.0–4955.0	−0.141	0.262
	5075.0–5175.0	+0.195	0.120
	6100.0–6200.0	+0.126	0.206
	6760.0–6800.0	+0.403	0.232
	7700.0–7800.0	+0.016	0.249

Table A14. Chemical abundances HHH86-30.

Element	Wavelength (Å)	Abundance	Error
[Fe/H]	4400.0–4600.0	−0.316	0.029
	4600.0–4800.0	−0.275	0.011
	4800.0–5000.0	−0.355	0.021
	5000.0–5200.0	−0.335	0.011
	6100.0–6300.0	−0.187	0.038
	6300.0–6500.0	−0.396	0.030
	6500.0–6700.0	−0.275	0.041
	6700.0–6800.0	−0.564	0.062
	7400.0–7550.0	−0.334	0.032
	8500.0–8700.0	+0.035	0.021
	8700.0–8850.0	−0.395	0.051
[Mg/Fe]	4300.0–4370.0	+0.240	0.058
	4690.0–4710.0	+0.129	0.073
	5150.0–5200.0	+0.371	0.046
	8777.0–8832.0	+0.231	0.047
[Ca/Fe]	4445.0–4465.0	−0.009	0.082
	6100.0–6128.0	+0.340	0.073
	6430.0–6454.0	+0.399	0.081
	6459.0–6478.0	−0.308	0.168
	8480.0–8586.0	−0.129	0.042
	8623.0–8697.0	−0.190	0.041
[Ti/Fe]	4270.0–4322.0	+0.062	0.089
	4440.0–4474.0	−0.170	0.090
	4650.0–4718.0	+0.281	0.066
	4980.0–5045.0	+0.421	0.059
	6584.0–6780.0	+0.372	0.092
[Na/Fe]	5670.0–5700.0	+0.199	0.138
	6148.0–6168.0	+0.390	0.203
[Cr/Fe]	4580.0–4640.0	−0.039	0.066
	4640.0–4675.0	+0.425	0.059
	4915.0–4930.0	+0.460	0.155
[Mn/Fe]	4450.0–4515.0	+0.268	0.120
	4750.0–4770.0	+0.130	0.099
[Ni/Fe]	4700.0–4720.0	+0.061	0.109
	4910.0–4955.0	+0.071	0.082
	5075.0–5175.0	+0.091	0.058
	6100.0–6200.0	+0.181	0.090
	6760.0–6800.0	+0.232	0.138
	7700.0–7800.0	−0.130	0.165

Table A15. Chemical abundances HHH86-39.

Element	Wavelength (Å)	Abundance	Error
[Fe/H]	4400.0–4600.0	−1.064	0.012
	4600.0–4800.0	−1.554	0.031
	4800.0–5000.0	−1.024	0.021
	5000.0–5200.0	−1.174	0.021
	6100.0–6300.0	−1.525	0.021
	6300.0–6500.0	−1.495	0.030
	6500.0–6700.0	−1.574	0.062
	6700.0–6800.0	−1.913	0.146
	7400.0–7550.0	−1.354	0.031
	8500.0–8700.0	−1.595	0.031
	8700.0–8850.0	−1.625	0.041
[Mg/Fe]	4300.0–4370.0	–	–
	4690.0–4710.0	–	–
	5150.0–5200.0	–	–
	8777.0–8832.0	–	–
[Ca/Fe]	4445.0–4465.0	+1.117	0.090
	6100.0–6128.0	+0.727	0.092
	6430.0–6454.0	+0.425	0.110
	6459.0–6478.0	+0.013	0.124
	8480.0–8586.0	+0.077	0.074
	8623.0–8697.0	+0.028	0.076
[Ti/Fe]	4270.0–4322.0	+0.437	0.089
	4440.0–4474.0	−0.004	0.120
	4650.0–4718.0	−0.650	0.144
	4980.0–5045.0	+0.266	0.084
	6584.0–6780.0	−0.702	0.282
[Na/Fe]	5670.0–5700.0	−0.032	0.125
	6148.0–6168.0	−0.191	0.282
[Cr/Fe]	4580.0–4640.0	−0.371	0.110
	4640.0–4675.0	−0.222	0.118
	4915.0–4930.0	–	–
[Mn/Fe]	4450.0–4515.0	−0.759	0.248
	4750.0–4770.0	−0.252	0.119
[Ni/Fe]	4700.0–4720.0	+0.357	0.117
	4910.0–4955.0	−0.043	0.128
	5075.0–5175.0	−0.153	0.095
	6100.0–6200.0	−0.442	0.148
	6760.0–6800.0	−0.335	0.162
	7700.0–7800.0	−0.565	0.140

Table A16. Chemical abundances K-029.

Element	Wavelength (Å)	Abundance	Error
[Fe/H]	4400.0–4600.0	−0.774	0.021
	4600.0–4800.0	−0.805	0.041
	4800.0–5000.0	−0.775	0.030
	5000.0–5200.0	−0.744	0.021
	6100.0–6300.0	−0.696	0.046
	6300.0–6500.0	−0.690	0.050
	6500.0–6700.0	−0.714	0.062
	6700.0–6800.0	−0.644	0.111
	7400.0–7550.0	−0.685	0.062
	8500.0–8700.0	−0.664	0.042
	8700.0–8850.0	−0.507	0.078
[Mg/Fe]	4300.0–4370.0	+0.767	0.074
	4690.0–4710.0	+0.358	0.114
	5150.0–5200.0	+0.406	0.046
	8777.0–8832.0	+0.317	0.061
[Ca/Fe]	4445.0–4465.0	−0.0435	0.141
	6100.0–6128.0	+0.513	0.080
	6430.0–6454.0	+0.360	0.118
	6459.0–6478.0	−0.437	0.248
	8480.0–8586.0	+0.168	0.025
	8623.0–8697.0	+0.138	0.025
[Ti/Fe]	4270.0–4322.0	−0.123	0.146
	4440.0–4474.0	−0.245	0.148
	4650.0–4718.0	+0.328	0.094
	4980.0–5045.0	+0.328	0.065
	6584.0–6780.0	+0.177	0.096
[Na/Fe]	5670.0–5700.0	+0.636	0.176
	6148.0–6168.0	+0.797	0.216
[Cr/Fe]	4580.0–4640.0	−0.153	0.095
	4640.0–4675.0	+0.298	0.084
	4915.0–4930.0	+0.707	0.212
[Mn/Fe]	4450.0–4515.0	−0.662	0.243
	4750.0–4770.0	+0.327	0.131
[Ni/Fe]	4700.0–4720.0	+0.238	0.144
	4910.0–4955.0	+0.258	0.113
	5075.0–5175.0	−0.3834	0.103
	6100.0–6200.0	+0.150	0.124
	6760.0–6800.0	+0.007	0.212
	7700.0–7800.0	−0.284	0.245

Table A17. Chemical abundances K-034.

Element	Wavelength (Å)	Abundance	Error
[Fe/H]	4400.0–4600.0	−0.534	0.012
	4600.0–4800.0	−0.485	0.030
	4800.0–5000.0	−0.596	0.024
	5000.0–5200.0	−0.534	0.012
	6100.0–6300.0	−0.654	0.031
	6300.0–6500.0	−0.594	0.035
	6500.0–6700.0	−0.445	0.049
	6700.0–6800.0	−0.604	0.081
	7400.0–7550.0	−0.535	0.042
	8500.0–8700.0	−0.325	0.021
	8700.0–8850.0	−0.305	0.054
[Mg/Fe]	4300.0–4370.0	+0.723	0.049
	4690.0–4710.0	+0.213	0.087
	5150.0–5200.0	+0.391	0.049
	8777.0–8832.0	+0.263	0.044
[Ca/Fe]	4445.0–4465.0	+0.014	0.097
	6100.0–6128.0	+0.164	0.077
	6430.0–6454.0	+0.471	0.090
	6459.0–6478.0	+0.064	0.152
	8480.0–8586.0	−0.007	0.031
	8623.0–8697.0	−0.027	0.032
[Ti/Fe]	4270.0–4322.0	+0.113	0.090
	4440.0–4474.0	+0.045	0.092
	4650.0–4718.0	+0.104	0.097
	4980.0–5045.0	+0.304	0.052
	6584.0–6780.0	−0.002	0.168
[Na/Fe]	5670.0–5700.0	+0.293	0.144
	6148.0–6168.0	+0.432	0.192
[Cr/Fe]	4580.0–4640.0	−0.017	0.068
	4640.0–4675.0	+0.403	0.060
	4915.0–4930.0	+0.614	0.185
[Mn/Fe]	4450.0–4515.0	+0.144	0.135
	4750.0–4770.0	+0.142	0.109
[Ni/Fe]	4700.0–4720.0	+0.233	0.124
	4910.0–4955.0	+0.447	0.087
	5075.0–5175.0	−0.227	0.085
	6100.0–6200.0	−0.087	0.112
	6760.0–6800.0	+0.267	0.154
	7700.0–7800.0	−0.107	0.202

Table A18. Chemical abundances K-163.

Element	Wavelength (Å)	Abundance	Error
[Fe/H]	4400.0–4600.0	−1.115	0.012
	4600.0–4800.0	−1.049	0.036
	4800.0–5000.0	−1.145	0.021
	5000.0–5200.0	−1.095	0.021
	6100.0–6300.0	−1.060	0.046
	6300.0–6500.0	−1.026	0.043
	6500.0–6700.0	−0.805	0.057
	6700.0–6800.0	−1.115	0.157
	7400.0–7550.0	−1.196	0.210
	8500.0–8700.0	−1.136	0.064
	8700.0–8850.0	−0.876	0.079
[Mg/Fe]	4300.0–4370.0	+0.867	0.051
	4690.0–4710.0	+0.289	0.128
	5150.0–5200.0	+0.448	0.048
	8777.0–8832.0	+0.527	0.057
[Ca/Fe]	4445.0–4465.0	+0.157	0.101
	6100.0–6128.0	+0.527	0.089
	6430.0–6454.0	+0.753	0.101
	6459.0–6478.0	+0.440	0.158
	8480.0–8586.0	+0.458	0.037
	8623.0–8697.0	+0.401	0.037
[Ti/Fe]	4270.0–4322.0	+0.077	0.107
	4440.0–4474.0	+0.146	0.101
	4650.0–4718.0	+0.338	0.079
	4980.0–5045.0	+0.328	0.060
	6584.0–6780.0	+0.254	0.096
[Na/Fe]	5670.0–5700.0	–	–
	6148.0–6168.0	+0.648	0.219
[Cr/Fe]	4580.0–4640.0	−0.083	0.089
	4640.0–4675.0	+0.097	0.107
	4915.0–4930.0	+0.547	0.253
[Mn/Fe]	4450.0–4515.0	−0.453	0.184
	4750.0–4770.0	−0.113	0.116
[Ni/Fe]	4700.0—4720.0	+0.126	0.164
	4910.0–4955.0	+0.146	0.120
	5075.0–5175.0	−0.223	0.079
	6100.0–6200.0	+0.438	0.111
	6760.0–6800.0	+0.387	0.191
	7700.0–7800.0	+0.637	0.179

Table A19. Chemical abundances VHH81-03.

Element	Wavelength (Å)	Abundance	Error
[Fe/H]	4400.0–4600.0	−0.234	0.012
	4600.0–4800.0	−0.135	0.021
	4800.0–5000.0	−0.166	0.021
	5000.0–5200.0	−0.165	0.021
	6100.0–6300.0	−0.175	0.035
	6300.0–6500.0	−0.205	0.040
	6500.0–6700.0	−0.344	0.071
	6700.0–6800.0	−0.094	0.062
	7400.0–7550.0	−0.263	0.042
	8500.0–8700.0	+0.005	0.011
	8700.0–8850.0	−0.045	0.053
[Mg/Fe]	4300.0–4370.0	+0.343	0.075
	4690.0–4710.0	+0.188	0.085
	5150.0–5200.0	+0.392	0.058
	8777.0–8832.0	+0.106	0.051
[Ca/Fe]	4445.0–4465.0	+0.203	0.091
	6100.0–6128.0	+0.359	0.079
	6430.0–6454.0	+0.410	0.098
	6459.0–6478.0	−0.505	0.207
	8480.0–8586.0	−0.156	0.045
	8623.0–8697.0	−0.217	0.044
[Ti/Fe]	4270.0–4322.0	−0.037	0.091
	4440.0–4474.0	+0.064	0.093
	4650.0–4718.0	+0.103	0.075
	4980.0–5045.0	+0.213	0.059
	6584.0–6780.0	−0.309	0.167
[Na/Fe]	5670.0–5700.0	–	–
	6148.0–6168.0	–	–
[Cr/Fe]	4580.0–4640.0	−0.126	0.075
	4640.0–4675.0	+0.286	0.076
	4915.0–4930.0	+0.874	0.157
[Mn/Fe]	4450.0–4515.0	−0.182	0.144
	4750.0–4770.0	+0.393	0.104
[Ni/Fe]	4700.0–4720.0	−0.277	0.156
	4910.0–4955.0	+0.075	0.100
	5075.0–5175.0	+0.132	0.081
	6100.0–6200.0	+0.033	0.110
	6760.0–6800.0	+0.232	0.175
	7700.0–7800.0	+0.398	0.161

Table A20. Chemical abundances VHH81-05.

Element	Wavelength (Å)	Abundance	Error
[Fe/H]	4400.0–4600.0	−1.643	0.053
	4600.0–4800.0	−1.683	0.072
	4800.0–5000.0	−1.564	0.042
	5000.0–5200.0	−1.465	0.051
	6100.0–6300.0	−1.403	0.083
	6300.0–6500.0	−1.623	0.092
	6500.0–6700.0	−2.074	0.111
	6700.0–6800.0	−1.653	0.313
	7400.0–7550.0	−1.413	0.123
	8500.0–8700.0	−1.944	0.071
	8700.0–8850.0	−1.423	0.163
[Mg/Fe]	4300.0–4370.0	+0.396	0.110
	4690.0–4710.0	+0.156	0.278
	5150.0–5200.0	+0.246	0.079
	8777.0–8832.0	−0.074	0.162
[Ca/Fe]	4445.0–4465.0	+0.227	0.211
	6100.0–6128.0	+0.487	0.182
	6430.0–6454.0	+0.266	0.239
	6459.0–6478.0	–	–
	8480.0–8586.0	+0.546	0.061
	8623.0–8697.0	+0.526	0.063
[Ti/Fe]	4270.0–4322.0	+0.356	0.162
	4440.0–4474.0	+0.456	0.154
	4650.0–4718.0	+0.277	0.163
	4980.0–5045.0	+0.507	0.110
	6584.0–6780.0	+1.176	0.154
[Na/Fe]	5670.0–5700.0	–	–
	6148.0–6168.0	–	–
[Cr/Fe]	4580.0–4640.0	−0.134	0.219
	4640.0–4675.0	−0.053	0.299
	4915.0–4930.0	–	–
[Mn/Fe]	4450.0–4515.0	−0.163	0.397
	4750.0–4770.0	−0.194	0.229
[Ni/Fe]	4700.0–4720.0	−0.753	0.725
	4910.0–4955.0	−0.454	0.982
	5075.0–5175.0	−0.465	0.219
	6100.0–6200.0	–	–
	6760.0–6800.0	−0.144	0.346
	7700.0–7800.0	−0.464	0.804

This paper has been typeset from a TEX/LATEX file prepared by the author.